APPROVAL PAGE FOR GRADUATE THESIS OR PROJECT

GS-13

SUBMITTED IN PARTIAL FULFILLMENT OF REQUIREMENTS FOR DEGREE OF MASTER OF SCIENCE AT CALIFORNIA STATE UNIVERSITY, LOS ANGELES BY

Sophia Iqbal
Candidate

Physics
Field of Concentration

TITLE: **Study of $^4He(e,e'p)^3H$ through the $(e,e'p)$ reaction at $Q^2 = 2(GeV/c)^2$ and $x_b = 1.24$**

APPROVED:	**Konrad A. Aniol** Committee Chairperson	Signature
	Martin B. Epstein Faculty Member	Signature
	Demetrius J. Margaziotis Faculty Member	Signature
	Oscar O. Bernal Department Chairperson	Signature

DATE: **December 9, 2013**

STUDY OF $^4He(e,e'p)^3H$ THROUGH THE $(e,e'p)$ REACTION AT $Q^2 = 2(GeV/c)^2$ AND $x_b = 1.24$

A Thesis

Presented to

The Faculty of the Department of Physics and Astronomy

California State University, Los Angeles

In Partial Fulfillment

of the Requirements for the Degree

Master of Science

in Physics

By

Sophia Iqbal

December 2013

ACKNOWLEDGMENTS

First and foremost, I would like to express my sincere appreciation and gratitude to my advisor, professor Aniol, for being such an excellent advisor. I began the masters program without a B.S. (I have a B.A. in sociology), and therefore very little formal knowledge of physics, and Konrad accepted me as a student in his lab. I am indebted to him for his constant advice, support, encouragement, guidance and patience. He gave me the tools I needed to perform the analysis and write this thesis. He made this dream of mine a reality.

I would secondly like to thank Fatiha Benmokhtar for teaching me how to do a large part of the analysis over the summer of 2011.

Thanks to Patricia Solvignon and Zhihong Ye for sharing their ztgt results with us and pointing out the possiblity to understand the structure in the ztgt spectra using CFD for the SRC target. Special thanks to Silviu Covrig for providing the CFD calculations.

Thanks to the SRC committee for helping and supporting me while I was visiting Jefferson Lab over the past few years. Recently, Doug Higinbotham and Vincent Sulkosky have helped me through the writing process during our conference calls and especially over e-mail.

Thanks to Nathaniel See for helping us with the analysis.

Thanks to my defense committee Dr. Epstein and Dr. Margaziotis for taking the time to review my thesis. Special thanks to Dr. Epstein for pushing me and providing much needed advice in the past several months.

DEDICATION

To my paternal grandfather who made me memorize the speed of light, argued with me about time travel, and told me about all the great physicists.

ABSTRACT

Study of $^{4}He(e,e'p)^{3}H$ through the $(e,e'p)$ reaction at $Q^{2}=2(GeV/c)^{2}$ and $x_{b}=1.24$

By

Sophia Iqbal

The structure and dynamics of ^{4}He can be studied through $^{4}He(e,e'p)$ coincidence measurements at high momentum transfers. Using the Hall A high resolution spectrometers and a cryogenic ^{4}He target, the SRC (short range correlation) and E08009 experiments held at Jefferson Lab in April 2011 measured the entire range of missing momentum from 0.0 GeV/c to 0.9 GeV/c. The observables of interest in this experiment (E08009) are the missing energy and missing momenta for producing the triton (^{3}H) ground state. This thesis concentrates on missing momentum values of 153 and 353 MeV/c. Cross sections are calculated and compared to theory.

TABLE OF CONTENTS

Chapter

LIST OF TABLES

Table

LIST OF FIGURES

Figure

CHAPTER 1

Introduction

The fundamental goal of nuclear physics is to understand the properties of atomic nuclei. While the first nuclear models were developed in the twentieth century, computer advancement and experimental techniques in recent decades allow nuclear physicists to probe deep into the nucleus at the level of the nucleon-nucleon force. Since it is now known that nucleons are composed of quarks, physicists can study how the quark degrees of freedom may play a role in nuclei. One can also study n-body forces in nuclei, for example, by measuring nuclear binding energies or, in the case of the SRC experiment, by studying multi nucleon exclusive reactions.

In the standard shell model, two body forces are added to explain the properties of nuclear levels. Also, we can compare two particles in a nucleus by transforming one wave function into a center of mass wave function and the other into a relative wave function, thereby providing a mathematical description of the correlation. Since conventional nucleon-nucleon models have always included a correlation between two particles, a new model should do the same. After identifying correlation effects in the data and classifying them as short range, a quark model may explain that correlations originate at the quark level, and not at the nucleon-nucleon level.

Experimental nuclear physicists have been interested in two-nucleon correlations for a long time. They have studied reactions such as $(e, e'NN)$ and (π^+, π^-), but additional reaction mechanism effects blur the correlation physics. There are constantly problems associated with meson-exchange currents, isobar excitations, and nucleons rescattering with the residual nucleus. Thus, there is a lack of clear-cut results regarding two-nucleon correlations.

Most recently, physicists have been studying $(e, e'p)$ and $(e, e'NN)$ reactions on few body nuclei. Today's nucleon-nucleon potentials yield exemplary wave functions because they accurately describe nuclear properties. Experimentally, we can now achieve values of missing momentum that lie well above the 200 MeV/c Fermi momentum of all nuclei, thanks to today's high-current, continuous beam accelerators. Nucleon momenta below the Fermi momentum are basically domianted by the long range nuclear well which largely confines these fermions to a 'box' of dimention $r_0 A^{1/3}$. Thus, nucleon-nucleon correlations must be important. The experiment described in this thesis, $^4He(e, e'p)^3He$, takes advantage of the continuous electron beam accelerator at Thomas Jefferson Laboratory. For the value $x_b = 1.24$ (defined in the next section), we expect that two-nucleon correlations will be revealed by a broad peak in the missing energy spectrum. Such a peak was seen in the ^3He measurement of $^3He(e, e'p)pn$ [2].

1.1 Electron Scattering: Why Electrons are Good for Nuclear Physics

Electron scattering is one of the cleanest means of probing nuclei because it allows for a variation of energy and momentum transfers with a probe that is sensitive to nucleon wave functions throughout the nuclear volume. Hadronic probes, because of strong absorption, are sensitive to nucleon wave functions mainly on the nuclear surface and beyond.

In the one photon exchange approximation, quantum electrodynamics (QED) describes the electromagnetic interaction as the beam electron exchanging a virtual photon with the nucleus. The hadronic interaction is much stronger than the electromagnetic interaction while the virtual photon can probe the entire nuclear volume.

Over the past few decades, a great deal of information on the single particle aspect of nuclear structure has been collected by means of elastic, inelastic (e, e') and quasi-elastic $(e, e'p; x_b \approx 1)$ scattering experiments. The results lead to firm constraints on the mean field description of nuclei. Fairly speaking, the one body properties of nuclei are now well known. x_b is a kinematic variable that gives the electron's view of the target from which it scattered. x_b is defined by the following (assuming scattering from a proton):

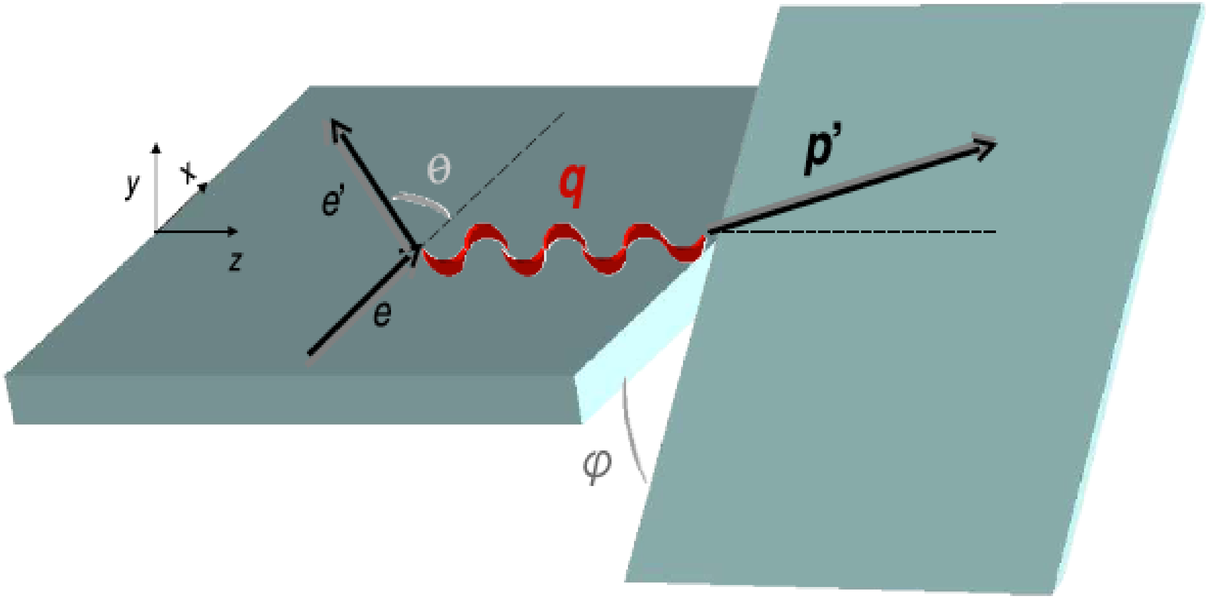

Figure 1.1: A schematic of the kinematics for the $(e, e'p)$ reaction

- $\underset{\sim}{e}$ = incoming electron momentum
- $\underset{\sim}{p} = 0$ = initial proton momentum
- $\underset{\sim}{e}'$ = outgoing electron momentum
- $\underset{\sim}{p}'$ = outgoing proton momentum
- E = initial total energy
- E' = final total energy
- E'_p = final proton energy
- m = mass.

Given that

$$e + p \longrightarrow e' + p', \tag{1.1}$$

$$\underset{\sim}{e} = \underset{\sim}{e}' + \underset{\sim}{p}' \tag{1.2}$$

(conservation of momentum), then

$$E = \sqrt{m_e^2 + e^2} + m_p \tag{1.3}$$

and

$$E' = \sqrt{m_e^2 + e'^2} + \sqrt{m_p^2 + p'^2}. \tag{1.4}$$

And given that

$$\underset{\sim}{q} = \underset{\sim}{e} - \underset{\sim}{e}' = \underset{\sim}{p}', \tag{1.5}$$

and

$$\omega = |e| - |e'|, \tag{1.6}$$

then

$$E'_p = m_p + \omega = \sqrt{m_p^2 + q^2}, \tag{1.7}$$

$$\cancel{m_p^2} + \omega^2 + 2\omega m_p = \cancel{m_p^2} + q^2, \tag{1.8}$$

$$2\omega m_p = q^2 - \omega^2, \tag{1.9}$$

and

$$1 = \frac{q^2 - \omega^2}{2m_p\omega} = \frac{Q^2}{2m_p\omega} = x_b. \tag{1.10}$$

In the mean field approximation, the proton is interacting on average with all the nucleons but is not interacting strongly with any single nucleon. But one of the observables of interest in nuclear physics is the strength of nucleon-nucleon correlations. This would mean that the proton struck by the electron is engaged in a short range interaction. In that case, for nucleon-nucleon correlations, the object the electron interacts with is more massive than an isolated proton. Suppose this correlated pair has an effective mass m_c. In the experiment we measure Q_c^2 and ω_c. We define the x_b as $x_c = \frac{Q_c^2}{2\omega_c m_p}$. But we know from kinematics that $\frac{Q_c^2}{2\omega_c m_c} = 1$. If we divide the first equation by the second, then $x_c = \frac{m_c}{m_p}$. For this experiment, the choice of $x_b = 1.24$ means that we are knocking out a proton interacting with a neighboring nucleon.

Because the one body properties of nuclei are well known:

- Increasing the momentum transfer allows one to probe the spatial structure of nuclei over the length of the nucleon or a smaller distance. This is the region in which short range correlations between nucleons are expected but poorly known, and the investigation of these correlations is a major goal of modern nuclear physics.
- The structure of hadrons must be taken into consideration at high momentum transfers. Using the nucleus as a laboratory, it is also a central goal to study the exchange of nucleonic and mesonic degrees of freedom with quarks and antiquarks. What are the effects of neighboring nucleons on a nucleon? Does it lose its identity within a large quark cluster? And if so, at which distance?

1.2 Exclusive Electron Scattering: (e,e'p)

Inclusive electron scattering experiments collect data from many channels, and it is difficult to evaluate the individual contributions of each channel. Therefore, exclusive electron scattering $(e, e'p)$ is preferable to inclusive electron scattering (e, e') in that one can fully identify the final state. Since only one channel collects data, the theoretical description of the reaction is comparatively simple.

Two spectrometers are employed in exclusive experiments. One spectrometer detects the scattered electron and the other a knocked out nucleon. This reaction is called $(e, e'p)$ if the knocked out nucleon is a proton. Four-momentum conservation makes it possible to determine the energy transfer to the nucleus if one is first able to measure the energies and momenta of the incoming electron, outgoing electron, and outgoing proton.

In 1962, Jacob and Maris were the first to suggest that quasielastic $(e,e'p)$ experiments could be an important experimental approach to examine the energy levels and shell structure of medium and light nuclei. Since then, many exclusive experiments have been performed at facilities like Saclay, NIKHEF-K, Mainz, Tokyo, MIT-Bates and JLAB. Experimental results prove that the $(e,e'p)$ reaction is an exemplary tool for researching the single-particle properties of nuclei constituents.

1.3 Mechanisms of the (e,e'p) Reaction

In order to understand the mechanism of the reaction thoroughly, an explanation of the $(e,e'p)$ scattering experiments must allow for several processes. Some processes are easier to handle than others. These include:

- **For incident and scattered electrons: Bremsstrahlung and coulomb distortion; energy loss.** An electron will travel through scattering chamber windows, the target, and the detector. During travel, the electron will lose some energy and alter its momentum. Thus, the asymptotic values of energy and momentum for the outgoing particles are different when measured at the interaction vertex than at the spectrometers. The customary plane wave description of the electrons is approximate, but the Coulomb potential of the nucleus changes the electron wave function. These effects are technically challenging, but QED provides a good theoretical description.

- **Electron-proton interaction.** The interactions between an electron and free nucleons may be different from the interactions between the electron and protons embedded in the nuclear medium. It is only possible to disentangle the nuclear medium's effect within a particular nucleon model.

- **For the target nucleus: The single particle structure.** Within the impulse approximation that is used here, it is only via the overlap function of the initial and final nuclear systems that the single particle structure of the target nucleus is sampled by the $(e, e'p)$ reaction. Extreme mean-field models provide a simple interpretation of the overlap function, but when correlations are considered the computation becomes difficult.

- **Final state interactions (FSI).** A complication in the theoretical calculations arises because of the interaction between the knocked out proton and the residual system. For a realistic comparison betweeen data and calculations, this interaction must be considered.

1.3.1 Plane Wave Born Approximation (PWBA)

In the Plane Wave Born Approximation (PWBA), Dirac plane waves describe the behavior of incident and scattered electrons. The interaction is mediated by the exchange of one single virtual photon, which is why the PWBA is also referred to as the one-photon exchange approximation. Figure 1.2 diagrams the $(e, e'p)$ reaction in PWBA. One can apply the PWBA to light and medium nuclei because of the smallness of the electromagnetic coupling constant.

The Distorted Wave Born Approximation (DWBA) handles the corrections for

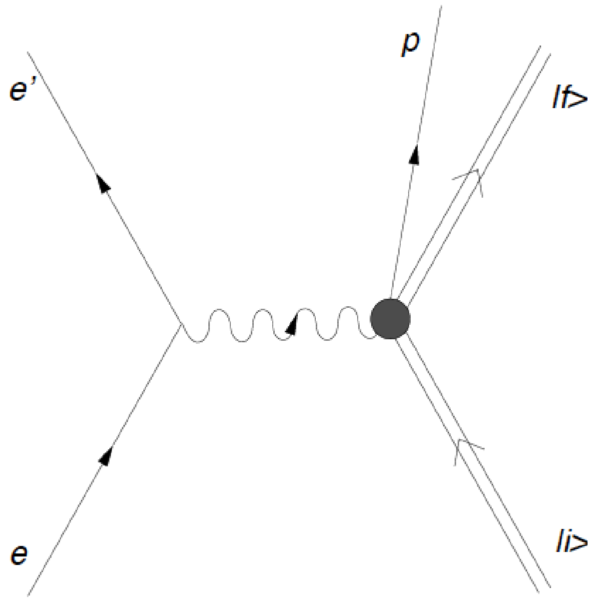

Figure 1.2: Feynmann diagram for $(e, e'p)$ in PWBA

the PWBA. A simple and relevant correction is to replace the electron's momentum transfer by an "effective momentum transfer" and maintain the rest of the PWBA formalism.

1.3.2 Plane Wave Impulse Approximation (PWIA)

In the Plane Wave Impulse Approximation (PWIA) it is assumed that a single bound nucleon absorbs the virtual photon. There is no further interaction with the nucleus and this nucleon is observed in the (e,e'N) measurement according to figure 1.3.

1.3.3 Distorted Wave Impulse Approximation (DWIA)

The Distorted Wave Impulse Approximation (DWIA) maintains the assumptions of the PWIA while taking final state interactions (FSI) into account. In this approximation, the ejected nucleon interacts with the residual nucleus through the strong interaction. Figure 1.4 diagrams the DWIA.

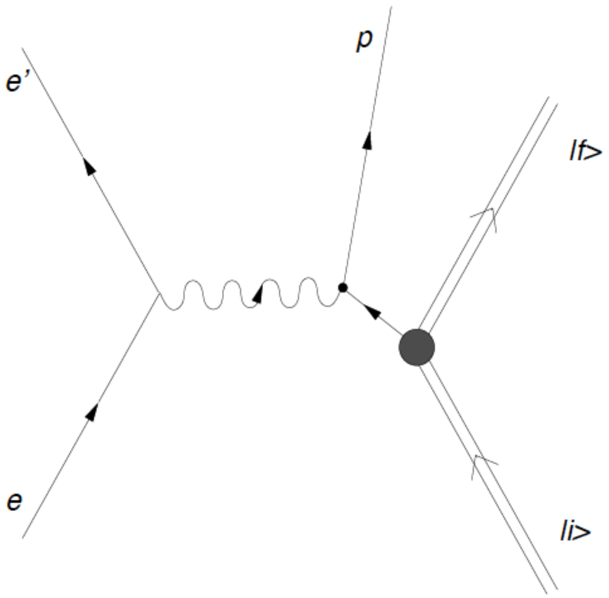

Figure 1.3: Feynmann diagram for $(e, e'p)$ in PWIA

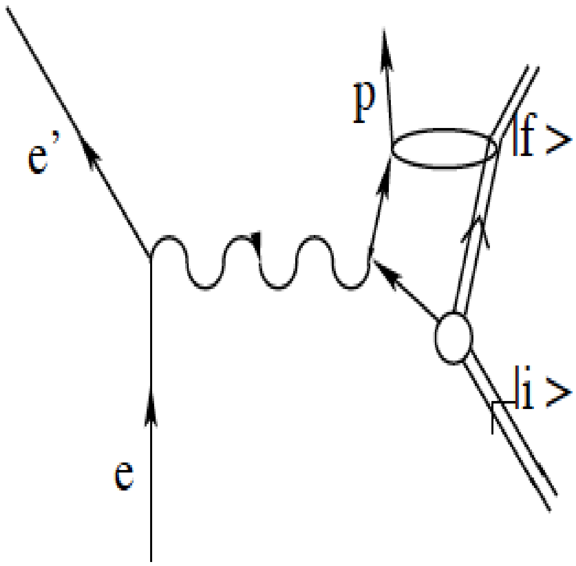

Figure 1.4: Diagram for $(e, e'p)$ in DWIA

The FSI are normally handled using an optical potential to obtain the distorted wave for the knocked out nucleon. Elastic nucleon-nucleus scattering data are fitted, and optical potentials are acquired from these fits. Optical potential formalism can be found in reference [12] (as cited in [2]).

1.4 Results From Previous $^4He(e,e'p)X$ Experiments

The SRC collaboration chose aspects of Hall A experiments 89-044, 97-111, and Hall B experiment 89-027/91-009 with the expectation of comparing these experiments to experiment e08009. Dr. Benmokhtar and Dr. Marat wrote their doctoral dissertations about Experiment 89-044, a $^3He(e,e'p)X$ experiment, from which the collaboration chose to use the same kinematic conditions, $\mathbf{q}$ = 1.5 GeV/c and ω = 0.84 GeV. However, the kinematical choice for ^4He (e08009) was different because it ran during the SRC experiment.

1.4.1 Study of the Quasielastic $^3He(e,e'p)$ Reaction at $Q^2 = 1.5\ (GeV/c)^2$ up to Missing Momenta of 1 GeV/c by Marat M. Rvachev

This dissertation concentrates on “the quasielastic $^3He(e,e'p)$ reaction in perpendicular coplanar kinematics, with energy and momentum transfer by the electron fixed at 837 Mev and 1500 MeV/c respectively, at three beam energies 1255, 1954 and 4807 MeV” (Marat, pp. 3). In the e08009 experiment, data for missing momentum kinematical settings 153, 353, 500, 625, and 755 MeV/c were measured and the beam energy was not varied. Dr. Rvachev studied the final state of the deuteron and proton-neutron, while this thesis concentrates on the final state of the triton. For the e08009 experiment, data are measured for Pmiss up to 1000 MeV/c, just as in Dr. Rvachev’s dissertation.

1.4.2 The Longitudinal and Transverse Response of the $(e, e'p)$ Reaction in Helium-3 and Helium-4 in the Quasielastic Region by Richard E.J. Florizone

When this experiment was conducted (1996-1998), the accelerator in Mainz Germany could only produce an 800 MeV electron beam. Considering this, there are a number of differences between the two experiments.

The Mainz experiment was performed in parallel kinematics, whearas the e08009 experiment was performed in perpendicular kinematics. $x_b = 0.90$ and $Q^2 = 0.41(GeV/c)^2$ for the Mainz experiment, while $x_b = 1.24$ and $Q^2 = 2(GeV/c)^2$ for the e08009 experiment. The Mainz experiment collected missing momentum values from 0-300 MeV/c. Only two of the e08009 kinematic values (resulting in a triton final state) are within this general range.

1.4.3 Measurement of the $^3He(e, e'p)pn$ Reaction at High Missing Energies and Momenta by Fatiha Benmokhtar

Jefferson Lab provided the high duty factor electron beam and 2 high precision spectrometers. The same beam and spectrometers were used for experiment e08009. Measurements were performed in perpendicular kinematics at fixed momentum ($|\vec{q}|$ = 1.5 GeV/c) and energy transfer (ω = 837 MeV) by the electron.

While Dr. Benmoktar's dissertation shows cross sections and spectral functions up to P_m =1 GeV/c and E_m =140 MeV (the pion production threshold), this thesis will only display cross sections of the ground state for 2 missing momenta kinematical settings. There is a bump in high missing energy for both experiments which follows kinematics expected for the virtual photon absorption on a nucleon pair, but I will not be investigating that here.

1.5 $^4He(e, ep)^3H$ Kinematics

The kinematics for an $(e, e'p)$ reaction is displayed below. The incoming and outgoing electrons define the scattering plane. Definitions are provided here:

- e is the incoming electron and is defined as $e = (E_e, \mathbf{e})$
- e' is the outgoing electron and is defined as $e' = (E'_e, \mathbf{e'})$
- $q = (w, \mathbf{q})$ is the four-momentum of the virtual photon
- $p' = (E_p, \mathbf{p'})$ is the four-momentum of the outgoing proton
- $(\mathbf{p}_m = \mathbf{q} - \mathbf{p'})$ is the missing momentum vector

"The four-momentum square, $Q^2 = q^2 - \omega^2$, is defined such that for electron scattering Q^2 is always positive" [1].

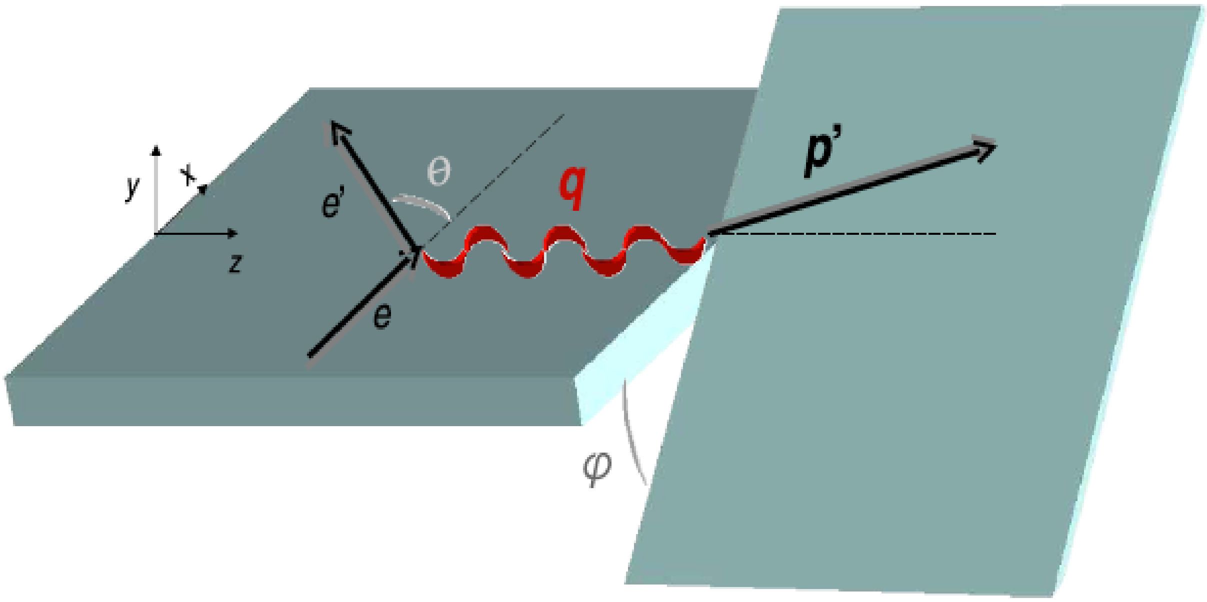

Figure 1.5: A schematic of the kinematics for the (e,e'p) reaction

CHAPTER 2

Motivation and Theory

2.1 Motivation

Traditionally, nucleons are described as point-like objects and nucleon form factors are added in as needed. However, since we now know that nucleons are composed of quarks, we can study whether the quark substructure of the nucleon affects nuclear structure. We assume that the long range attractive force is dominated by pion exchange between nucleons. We also assume that the short range repulsive force may need to be described by quark/gluon degrees of freedom. In order to find quark effects, short range correlations between nucleons must be studied. SRCs correspond to the high momentum region of the wave function. It is now possible to study this phenomenon with few body nuclei, which are particularly attractive since few body systems are increasingly amenable to microscopic theoretical treatments.

^4He has a similar density to that of heavier nuclei. Therefore, we can perform electron scattering experiments on it and expect the nucleon pairs to behave as they would inside massive nuclei. ^4He is also tightly bound and has strong correlations. These aspects provide a good environment to study nucleon-nucleon and short range correlations. We can simultaneously perform two and three body calculations also, and find a connection between the two if possible. These calculations would not be possible in lighter nuclei, where there are not enough pairs for three body calculations, or in heavier nuclei, where there are too many pairs. Perhaps in the future we will have formulated a complex code that can handle many body calculations, but we do not have the technology as of yet. So we use ^4He as a many body emulator.

^4He is a small enough system such that we can use it in variational Monte Carlo techniques, yet still large enough such that we can treat it as a mean field. While the former approach allows us to study the microscopic details of nuclear structure, the latter is used to understand general nuclear properties common to all nuclei with the same central density. One can say that the mean field provides a backbone to our understanding of nuclear structure. Deviations from the mean field predictions are attributed to nucleon correlations. Earlier studies of $^3He(e,e'p)$ employed scattered electrons where $x_b = 1$. In that case, the kinematics of the electron scattering is consistent with the electron scattering from a quasi-free proton, which is as close as one could expect to come to a proton subjected to the mean field. In our case $x_b = 1.24$, so the detected proton has an enhanced probability to have been struck while interacting with another nucleon. We have the ability to compare the experimental results with both a relativistic mean field approach to nuclear structure and with a non-relativistic mean field approach augmented with models of nucleon-nucleon correlations. Where a large data set is available, both techniques have been effectively utilized to explain electromagnetic interactions at a few hundred MeV/c of transferred momentum.

2.2 Theory

The relativistic mean field calculations are performed with the code produced by J.M. Udias [5]. In this code, a bound state wave function, the solution to the Dirac equation, is employed by using standard Wood-Saxon (WS) wells for the scalar (S) and vector (V) potentials. The WS potential parameters are fitted to the ^4He binding energy and measured rms radius; and predict the $^4He(e, e'p)^3H$ momentum distribution. Using the Dirac equation, a general solution of a bound particle always has a negative energy component, which is not the case for a free nucleon. In an entirely relativistic computation, the spinors are regularly described as being “distorted” because scalar and vector potentials appear in the negative component. The Udias code always calculates DWIA or PWIA using relativistic kinematics. Proton distortions are calculated by using an optical potential to solve the Dirac equation.

Nonrelativistic options are not used because although one can remove the relativistic dynamics from the wave functions, the operator and kinematics are still relativistic. Also, Hall A results for response functions and the A_{TL} symmetry from $^{16}O(e, e'p)^{15}N$ were satisfactorily described by Udias' full relativistic calculation [1].

CHAPTER 3

Experimental Setup

3.1 Coordinate Systems

An overview of the coordinate systems used in this experiment is presented. The coordinate systems presented are cartesian, and an angular coordinate refers to the tangent of the angle in question.

3.1.1 Hall A Coordinate System (HACS)

A top view of the Hall A coordinate system is shown in figure 3.1. The origin is defined by the intersection of the electron unrastered beam, centered in the last three beam position monitors (BPMs), and the target assembly's vertical symmetry axis of rotation. The $\hat{z}$ axis points along the beam line in the direction of the beam dump, $\hat{y}$ is vertically upward, and $\hat{x} = \hat{y} \times \hat{z}$.

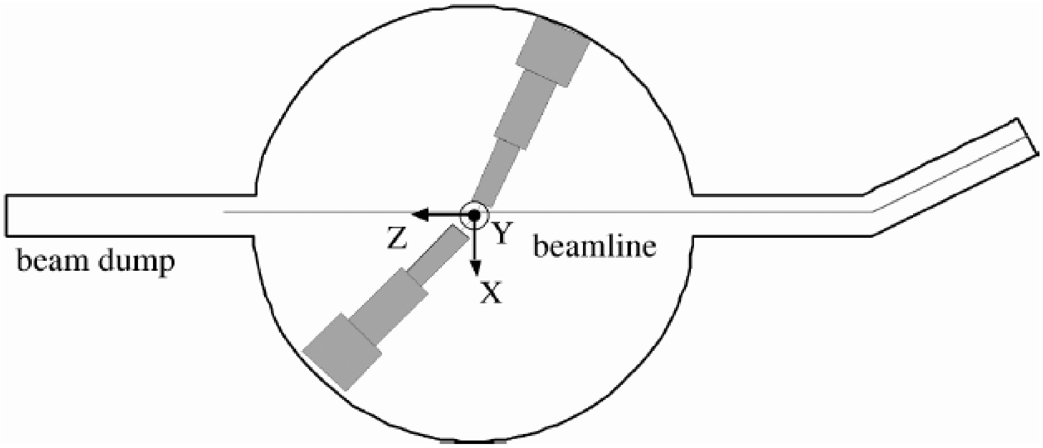

Figure 3.1: Hall A Coordinate System

3.1.2 Target Coordinate System (TCS)

Both spectrometers have their own TCS. The z axis of the TCS is defined by a line perpendicular to the sieve slit surface of the spectrometer and going through the midpoint of the central sieve slit hole as shown in figure 3.2. The x axis is defined by a line crossing the center of the sieve slit and pointing downward; $y = z \times x$. The triplet $\hat{x}, \hat{y}$, and $\hat{z}$ is right handed. Ideally the origin of the TCS should coincide with the origin for the HACS and the center of the rotation of the spectrometer, but the $x - z$ plane incorporates the y axis of the HACS. Subscripts with the designation "tg" or "tgt" refer to the target. The x and y axis define a plane where variables x_{tg} and y_{tg} are the x and y coordinates of a particle's point of intersection with this plane. The variables θ_{tg} and Φ_{tg} are defined as $\theta_{tg} = tan^{-1}\frac{dx}{dz}$ and $\Phi_{tg} = tan^{-1}\frac{dy}{dz}$.

3.2 CEBAF Accelerator

The E08009 experiment was performed in Hall A at the Thomas Jefferson National Accelerator Facility (TJNAF) on April 13 and 14 of 2011. This was a coincidence experiment, with the scattered electrons detected in the electron arm High Resolution Spectrometer (LHRS) and the knocked out proton detected in the Hadron High Resolution Spectrometer (RHRS).

A diagram of the accelerator site is shown in figure 3.3. The accelerator can accelerate electrons to 6 GeV with beam currents up to 100 μA.

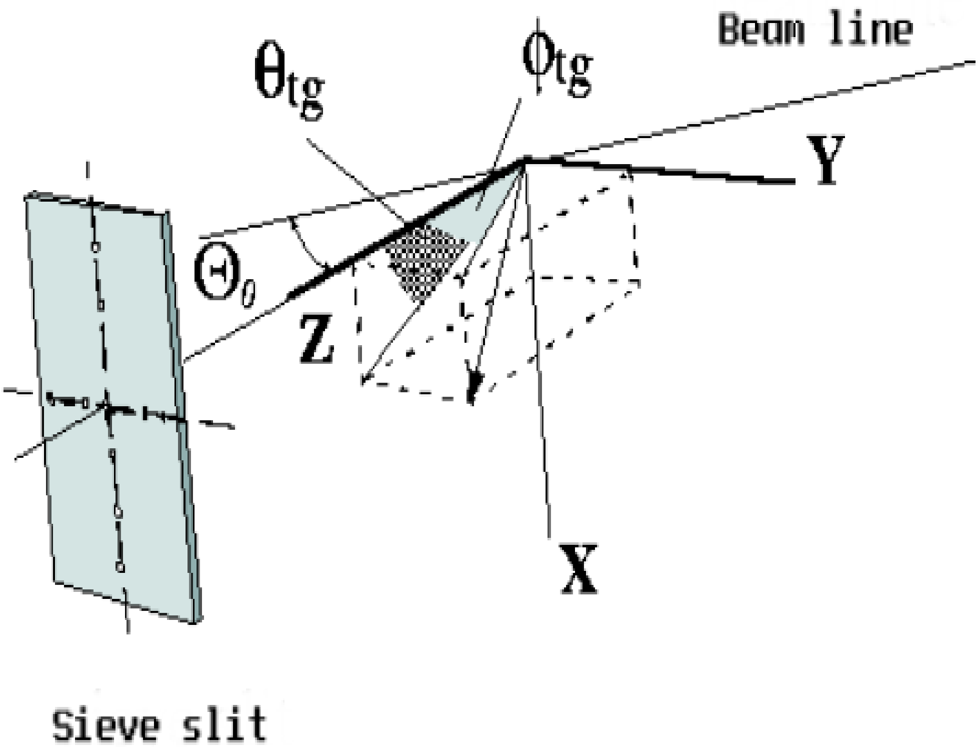

Figure 3.2: Target Coordinate System

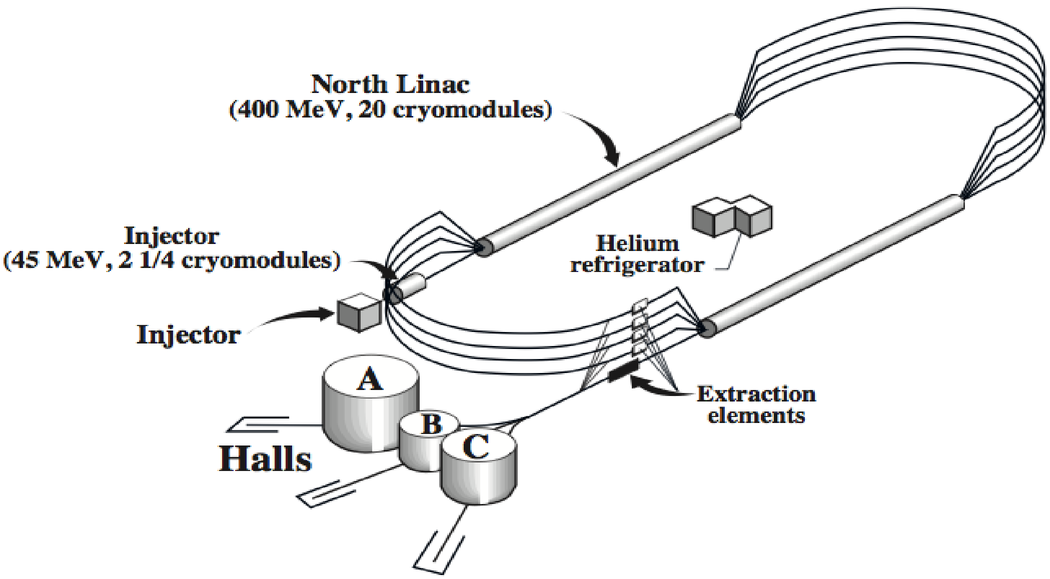

Figure 3.3: Layout of Jefferson Lab accelerator site

3.3 Hall A Spectrometers

The Hall A spectrometers are designed for the detailed investigation of nuclear structure, often employing the $(e, e'p)$ reaction. The measurements widen the range of momentum transfer and internal nucleon momenta over those of earlier measurements at other laboratories.

These identical $4GeV/c$ spectrometers are the chief components of the Hall A equipment. Their basic layout is shown in figures 3.4, 3.5, 3.6, and 3.7. Starting from the center of figure 3.5 and bending vertically upward, there are:

1. a pair of superconducting $\cos(2\theta)$ quadrupoles.
2. a 6.6 m long-dipole magnet with focussing entrance and exit pole faces, including supplementary focussing from a field gradient, n, in the dipole.
3. a 3rd superconducting $\cos(2\theta)$ quadrupole.

The second and third quadrupoles of each spectrometer are duplicates in terms of design and construction because they have similar field and size requirements. The major design features of the spectrometers are shown in table 3.1.

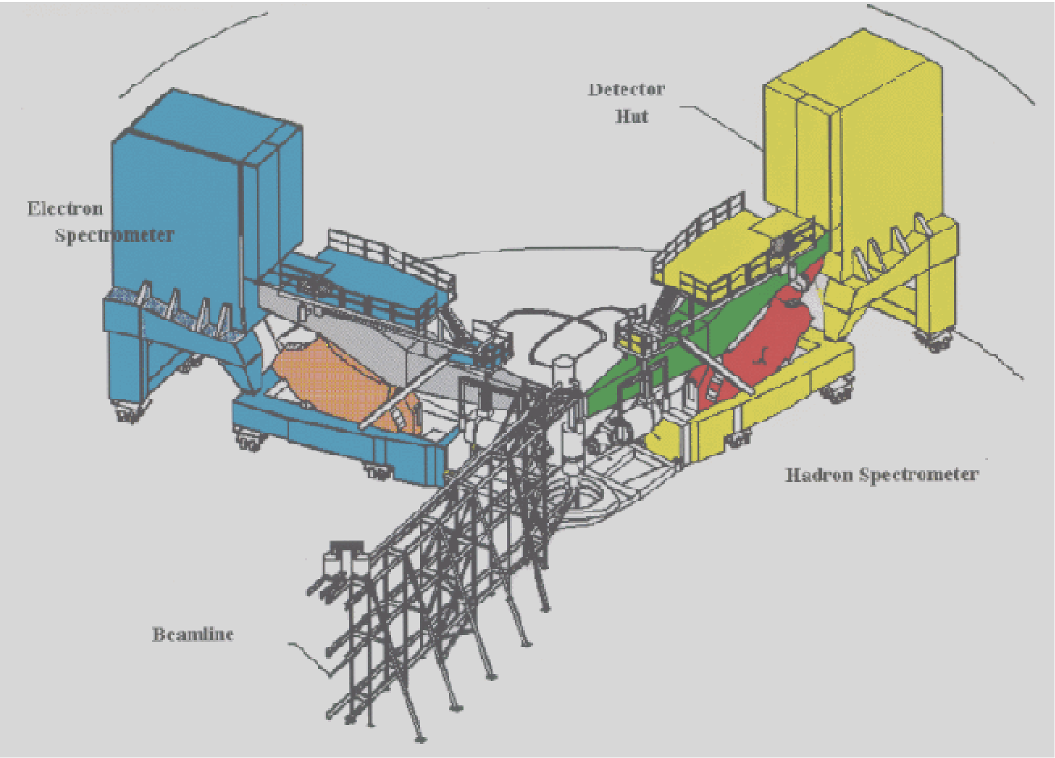

Figure 3.4: Bird's-eye view of Hall A Spectrometers

3.4 Target: Why a Cryogenic Target was Used

Since ^4He is close to being an ideal gas, the ideal gas law $\frac{n}{V} = \frac{P}{RT}$ is a useful first approximation. According to this law, when pressure and volume are fixed, decreasing the temperature will increase the number of moles (or the number or nuclei) in a given volume. Thus, decreasing the temperature of a target allows us to increase the number of nuclei.

Table 3.1: Hall A High Resolution Spectrometers General Characteristics

Momentum Range	0.3 - 0.4 GeV/c
Configuration	QQDQ
Bend Angle	45 degrees
Optical Length	23.4 m
Momentum Acceptance	+/- 4.5 %
Dispersion (D)	12.4 cm/%
Radial Linear Magnification (M)	2.5
D/M	5
Momentum Resolution (FWHM)	1×10^{-4}
Angular Acceptance:	
Horizontal	+/- 28 mr
Vertical	+/- 60 mr
Solid Angle:	
(rectangular approximation)	6.7 msr
(elliptical approximation)	5.3 msr
Angular Resolution: (FWHM)	
Horizontal	0.6 mr
Vertical	2.0 mr
Transverse Length Acceptance	+/- 5 cm
Transverse Position Resolution (FWHM)	1.5 mm
Spectrometer Angle Determination Accuracy	0.1 mr

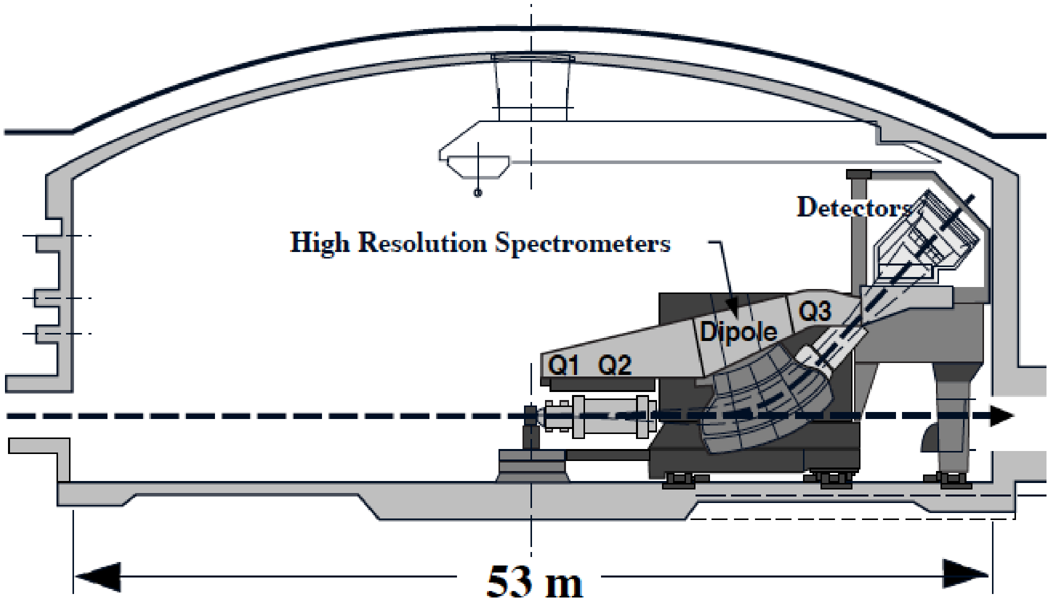

Figure 3.5: Side view of one of the Hall A spectrometers

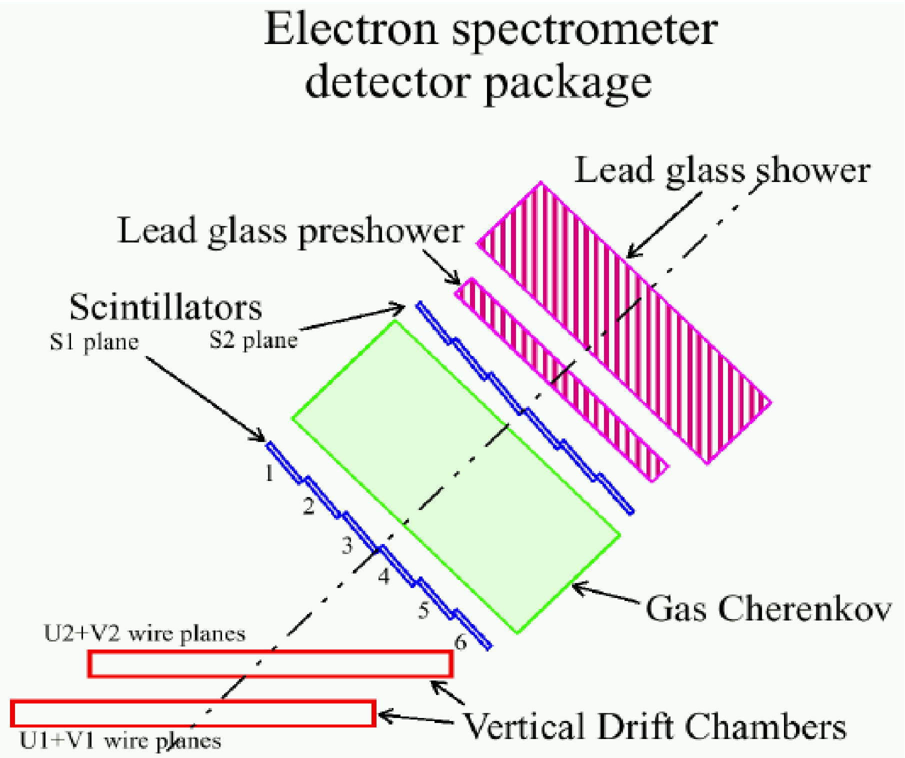

Figure 3.6: Electron Arm Package

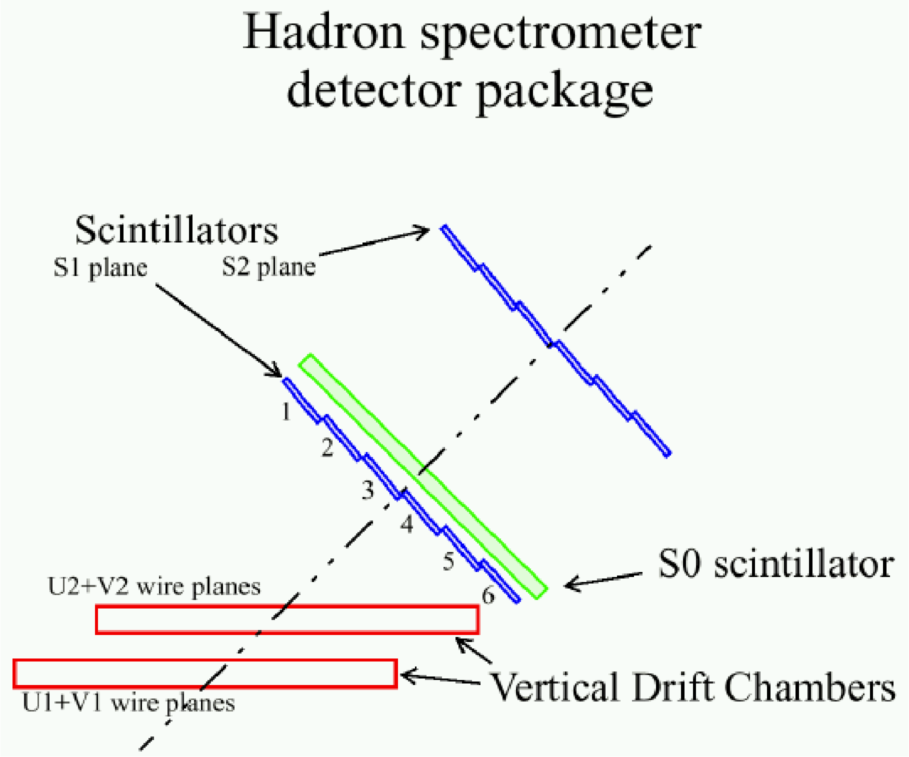

Figure 3.7: Hadron Arm Package

CHAPTER 4

Detector Calibration: Time Parameters and Efficiencies

4.1 Coincidence Time of Flight

The coincidence time of flight spectrum is the measure of the time of flight difference between the electron in the left HRS and the proton in the right HRS. Random coincidence events are events that originate from anywhere, while true coincidence events originate from a single nucleus. 20 bins are chosen to envelope and cut off the true plus random timing peak. Starting from the left and right ends of this cut, 40 more bins are cut on either side to justify the random cuts. Specific parameters are listed for each kinematic value under its plot. The randoms are subtracted from the trues according to the following equation:

$$(trues + randoms) - \frac{1}{4} randoms = trues. \tag{4.1}$$

4.2 Computer and Electronic Dead Time

There are two types of dead time; computer dead time (CDT) and electronic dead time (EDT). CDTs and EDTs are the time after each event during which the system is not able to record another event.

4.2.1 Computer Dead Time

The DAQ (data acquisition system) experiences a “dead time” when more events are produced than recorded, i.e. when the DAQ is already recording another event. The

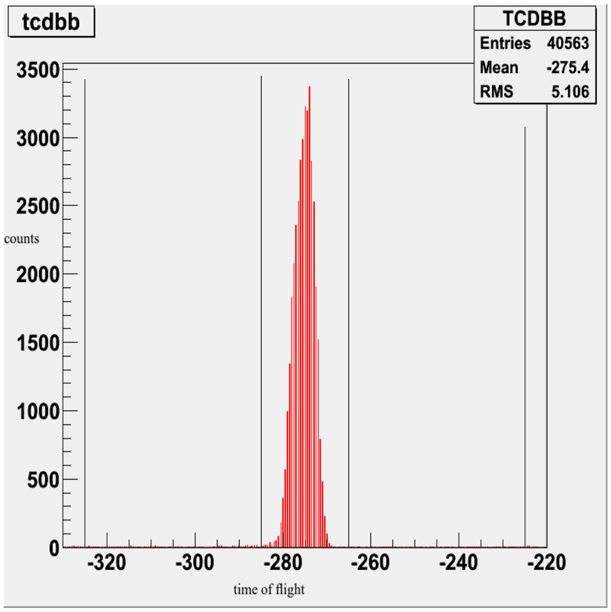

Figure 4.1: 153 MeV/c timing cuts. Trues + randoms measured from -285 to -265; randoms measured from -325 to -285 and -265 to -225.

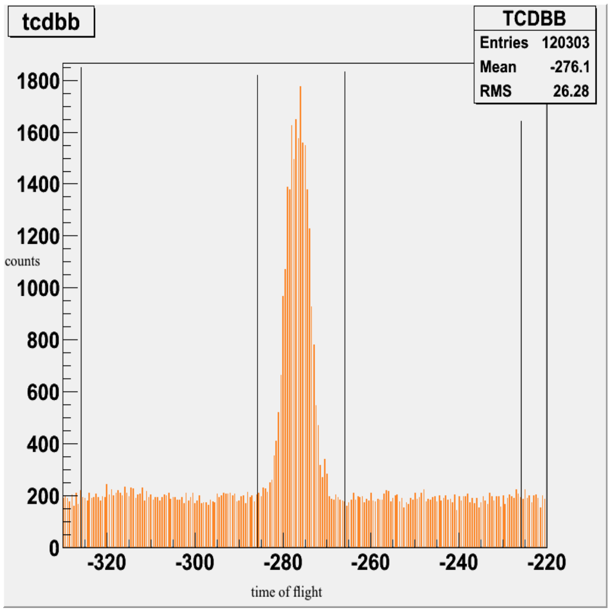

Figure 4.2: 353 MeV/c timing cuts. Trues + randoms measured from -286 to -266; randoms measured from -326 to -286 and -266 to -226.

computer dead time arises because of this inability in the DAQ system. Scalers count the total number of events for each type of event i (i=1,...,5) and this allows one to correct for the number of non-recorded events. The computer deadtime is respectively 0.08421 and 0.05048 for 153 and 353 MeV/c, with an uncertainty of 0.1 [2].

4.2.2 Electronic Dead Time

Given the non-zero time widths of digital signals, the electronic dead time is a result of the superposition of two or more signals. It becomes significant if the rates are high. The electronic deadtime study was not done for this thesis, but we can use a plot from Jones' report [11] (as cited in [2]) to estimate the electronic deadtime (since the electronics setup is the same). This plot is shown in figure 4.3. In general, the hadron and electron strobe rates for any given run (for our two kinematics) total less than 15 kHz. Thus, according to figure 4.3, the electronic deadtime is so small that it is negligible.

4.3 Trigger Efficiency

Triggers are generated based on scintillator signals and scintillator inefficiency causes trigger inefficiency. Scintillator inefficiency occurs because for the following reasons:

- A small amount of energy is deposited by the charged particles into the scintillator paddles, causing statistical fluctuations.
- Light is emitted by the particles in the paddles and is imperfectly transferred to the photo multiplier tubes (PMTs).
- There are PMT inefficiencies, and

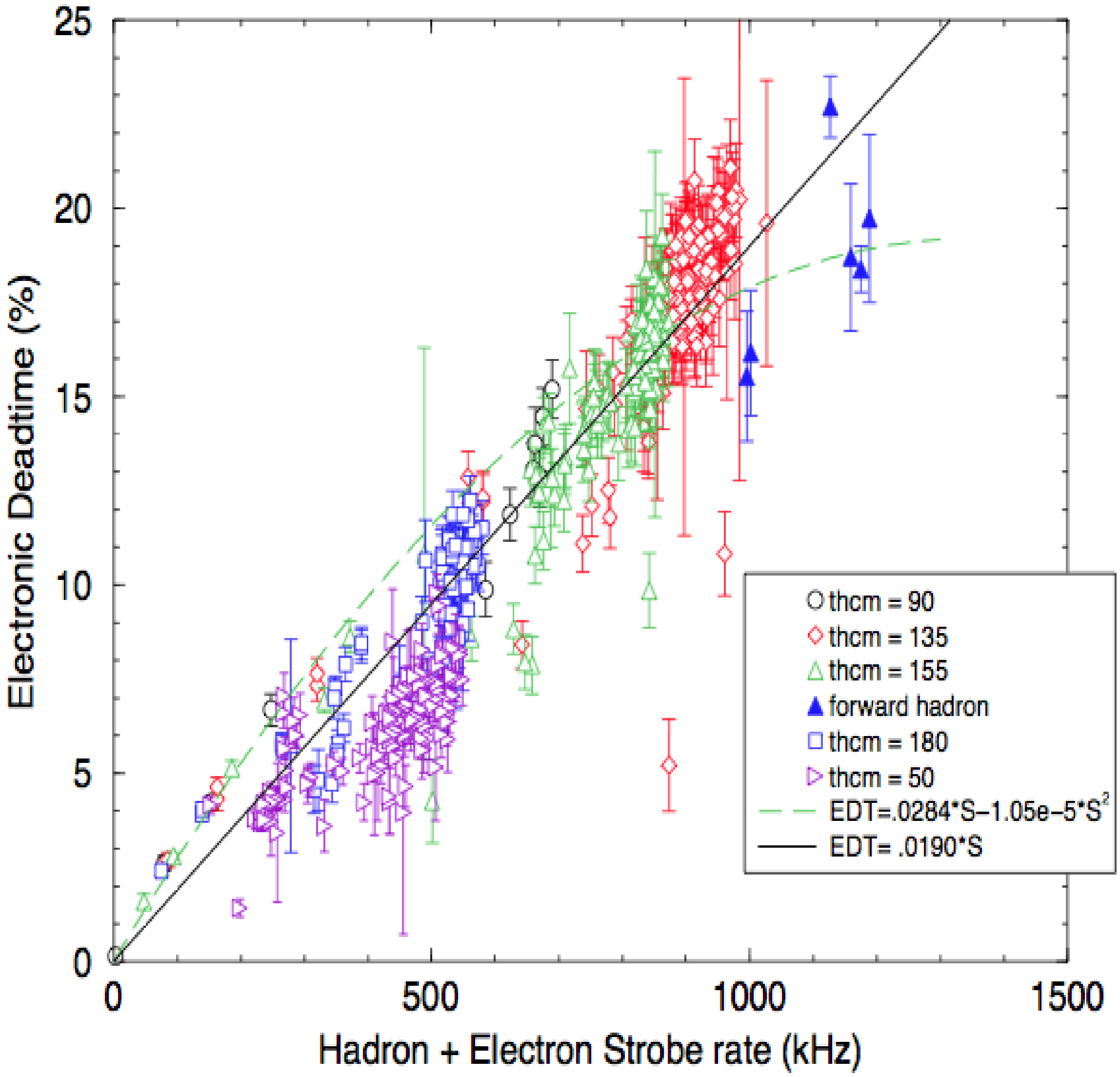

Figure 4.3: Graph of electronic deadtime from Jones' report [11] (as cited in [2]).

- other inefficiencies.

If trigger types 1, 3, and 5 (T1, T3, and T5) miss counting an event due to trigger inefficiency, it is most often counted by T2 in the electron spectrometer or T4 in the hadron spectrometer; the latter types allow for the calculation of trigger efficiencies.

Since time is limited in performing the analysis, the trigger efficiency is recorded from another Hall-A experiment. For Hall A experiment E06-007 [9], the lowest recorded trigger efficiency is 0.97 +/- 0.01.

4.4 Wire Chamber and Tracking Efficiency

The efficiency of a single sense wire in the wire chambers is the likelihood that the wire fires when a charged particle travels sufficiently close to it. It can be calculated according to the formula

$$\epsilon_{wire} = \frac{N_1}{N_0 + N_1}, \tag{4.2}$$

where N_1 is the number of times the wire fired and N_0 is the number of times the wire did not fire when, in both instances, two adjacent wires fired. This formula, however, does not take into account the case where different particles produce clusters of hit wires with a gap of one wire in between. Therefore, this efficiency formula constitutes a lower bound. To exclude other poorly constructed events from the analysis, tracking cuts are imposed.

The tracking efficiency for events of type i is calculated according to formula

$$\epsilon_{tr,i} = \frac{N_{i\prime}}{N_i}, i = 1, 3, 5, \tag{4.3}$$

where N_i is the total number of recorded events of type i and N_i' is the number of events of type i within the parameters of the tracking cuts.

Since time is limited in performing the analysis, the wire chamber and tracking efficiencies are recorded from another Hall A experiment. For Hall A experiment E06-007 [9], the average wire chamber efficiency is 0.9955 +/- 0.001 and the average tracking efficiency is 0.9895 +/- 0.0075.

CHAPTER 5

Data Analysis - Overview

5.1 Cuts

The experiment included kinematic values 153, 353, 500, 625 and 755 MeV/c. The E_{miss} plots displayed in figures 5.1-5.3 show that a sharp peak occurs for 153, 353 and 500 MeV/c. Going forth into the analysis, however, I consider only the first two kinematic values because these peaks are large enough where an analysis is feasible. The cuts outlined in this section are summarized in table 5.3.

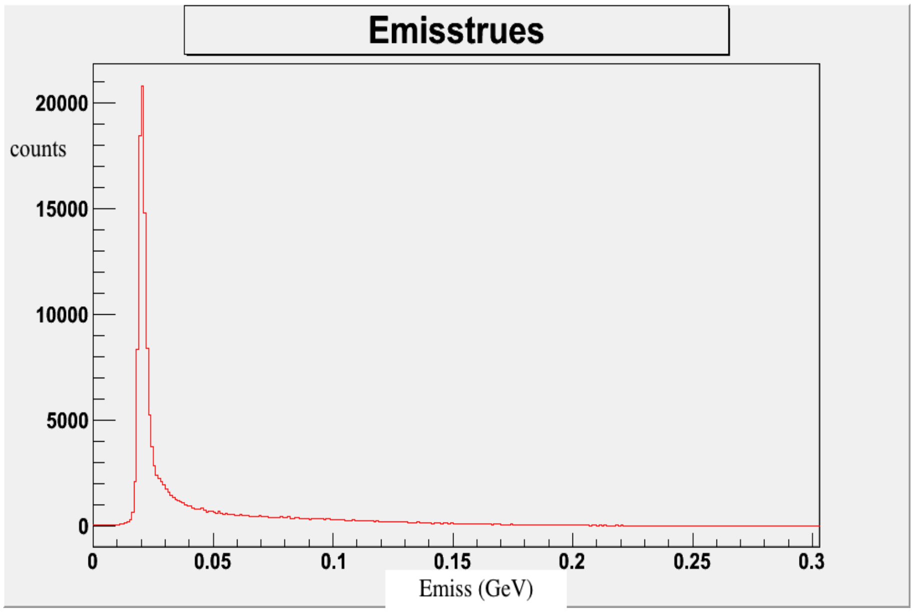

Figure 5.1: This plot shows the triton peak for kinematic value 153 MeV/c.

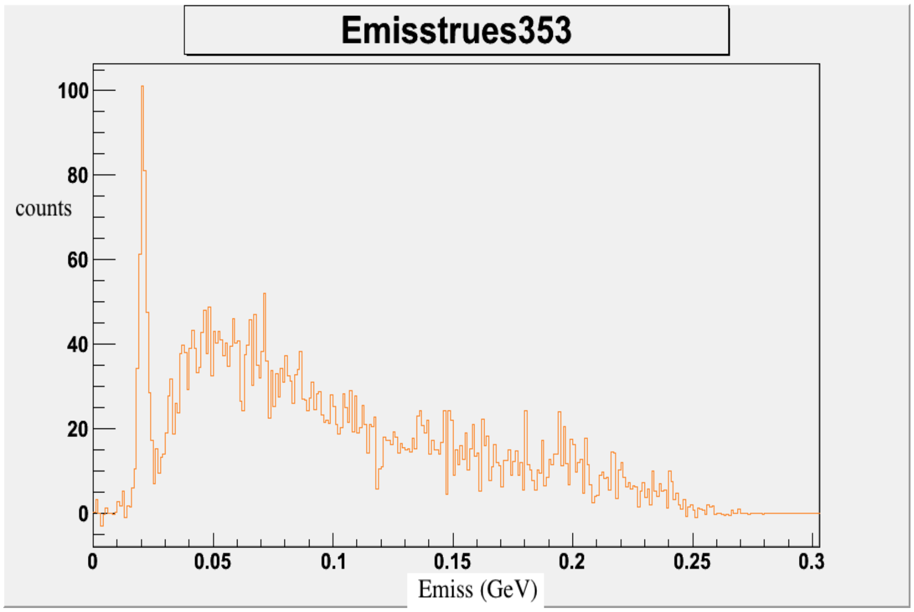

Figure 5.2: This plot shows the triton peak for kinematic value 353 MeV/c.

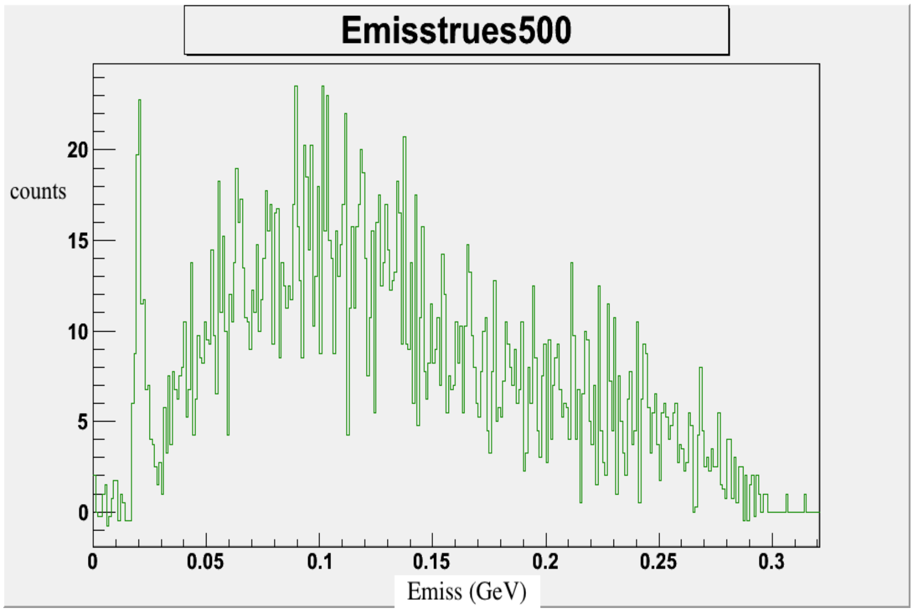

Figure 5.3: This plot shows the triton peak for kinematic value 500 MeV/c.

5.1.1 Angles

The angular acceptance of the spectrometers is +/- 60 mr vertically and +/- 28 mr horizontally. The simulation shows these values in figures 5.6 and 5.7. ϕ corresponds to the horizontal angle and θ corresponds to the vertical angle. Cuts are placed on angle θ at +/-0.04 radians and ϕ at +/-0.03 radians for kinematic values 153 and 353 MeV/c. Refer to figures 5.4-5.5 for the data plots.

5.1.2 Ztarget

Figures 5.8 and 5.9 show the electron beam along the z-axis. Cuts are placed at +/- 8 cm.

5.1.3 Deviation in Central Momentum

Cuts are placed at +/- 0.06 MeV/c for the deviation in the central momentum. Plots are shown figures 5.10 and 5.11 and table 5.3.

5.2 Density Measurement

The target employed for the SRC experiment required special treatment when making beam heating corrections for absolute cross section determinations for the high current runs needed for E08009. Using the left HRS (LHRS), which was maintained at a fixed momentum and angle setting during the joint E08009/E07006 experiments, it was possible to make density corrections along the beam path in the 20cm long ^4He cryogenic target. Additionally, we are able to compare the measured counts/Coulomb along the beam's path with computational fluid dynamic calculations(CFD) provided by Silviu Covrig [3].

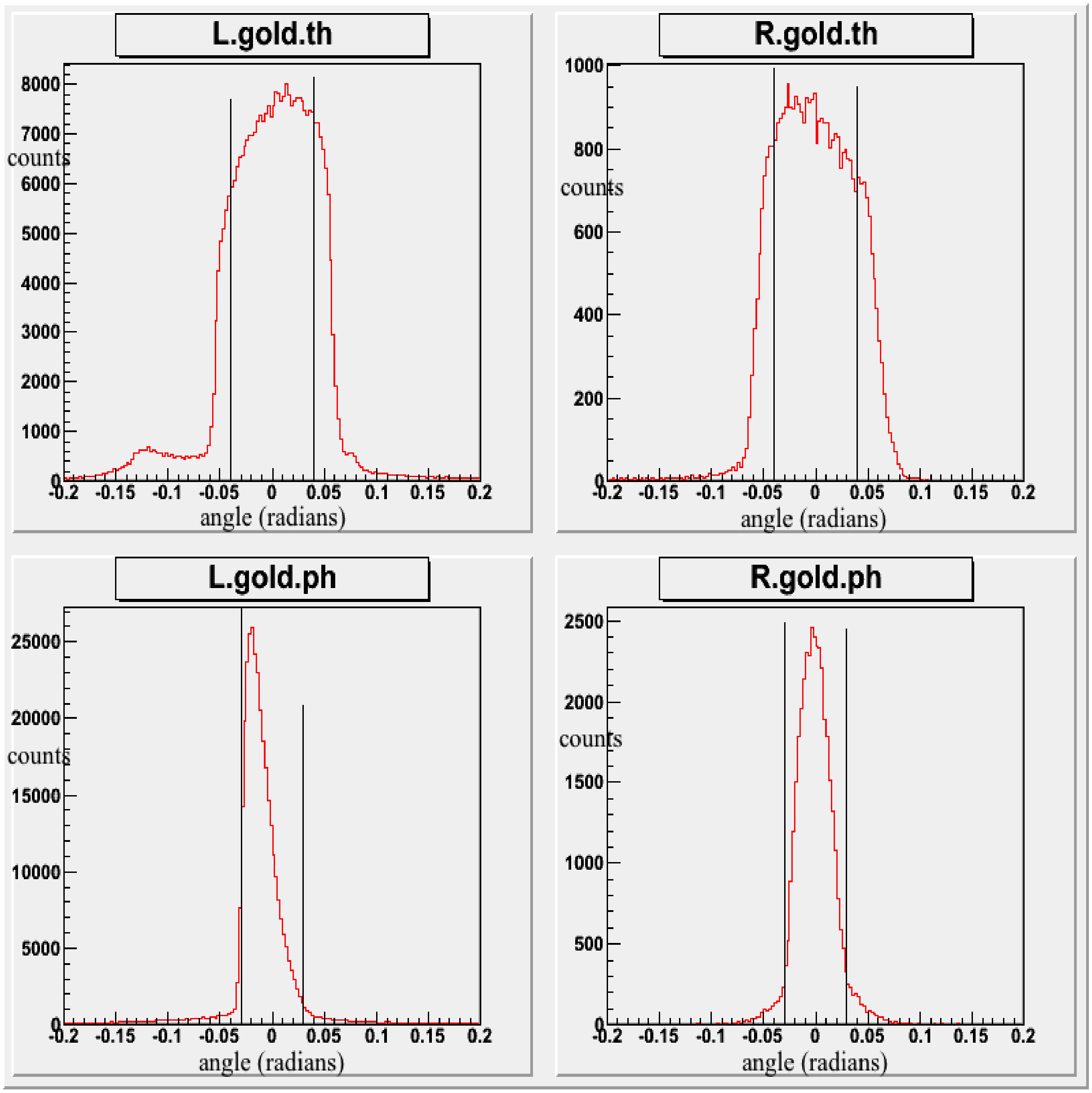

Figure 5.4: 153 MeV/c angle cuts placed at θ = +/-0.04 radians and ϕ = +/-0.03 radians.

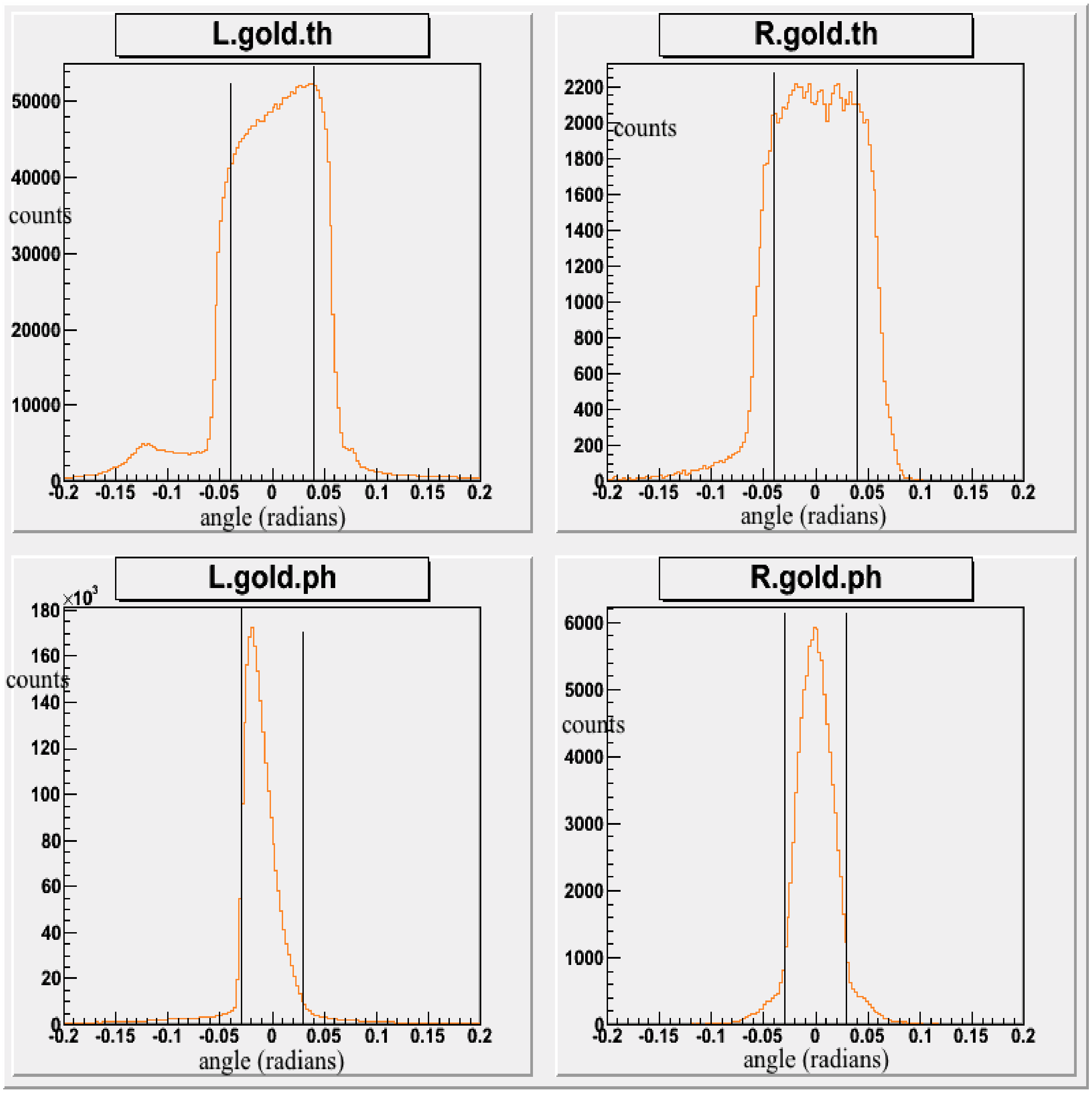

Figure 5.5: 353 MeV/c angle cuts placed at θ = +/-0.04 radians and ϕ = +/-0.03 radians.

θ.

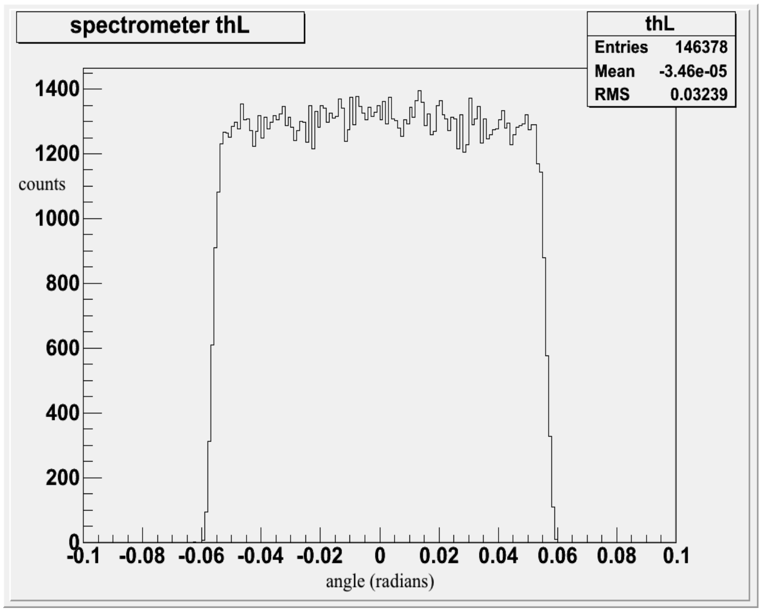

Figure 5.6: Angular spectrometer acceptance GEANT simulation for vertical angle θ.

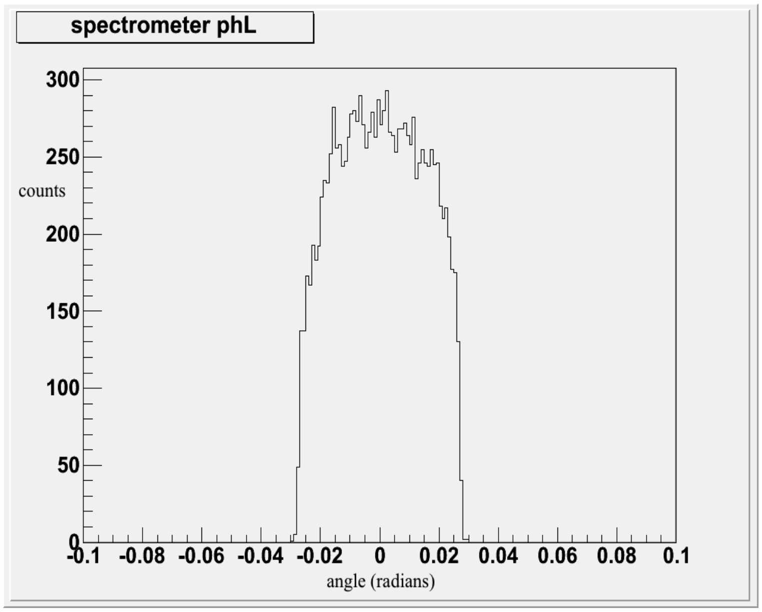

Figure 5.7: Angular spectrometer acceptance GEANT simulation for horizontal angle ϕ.

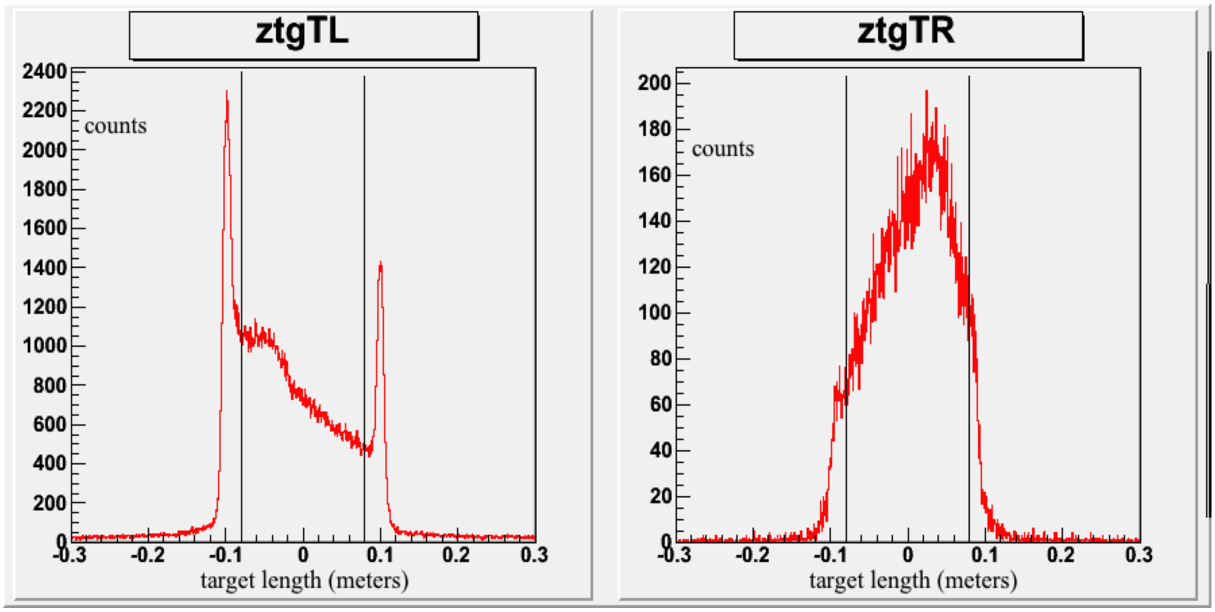

Figure 5.8: 153 MeV/c ztarget cuts placed at +/- 8 cm.

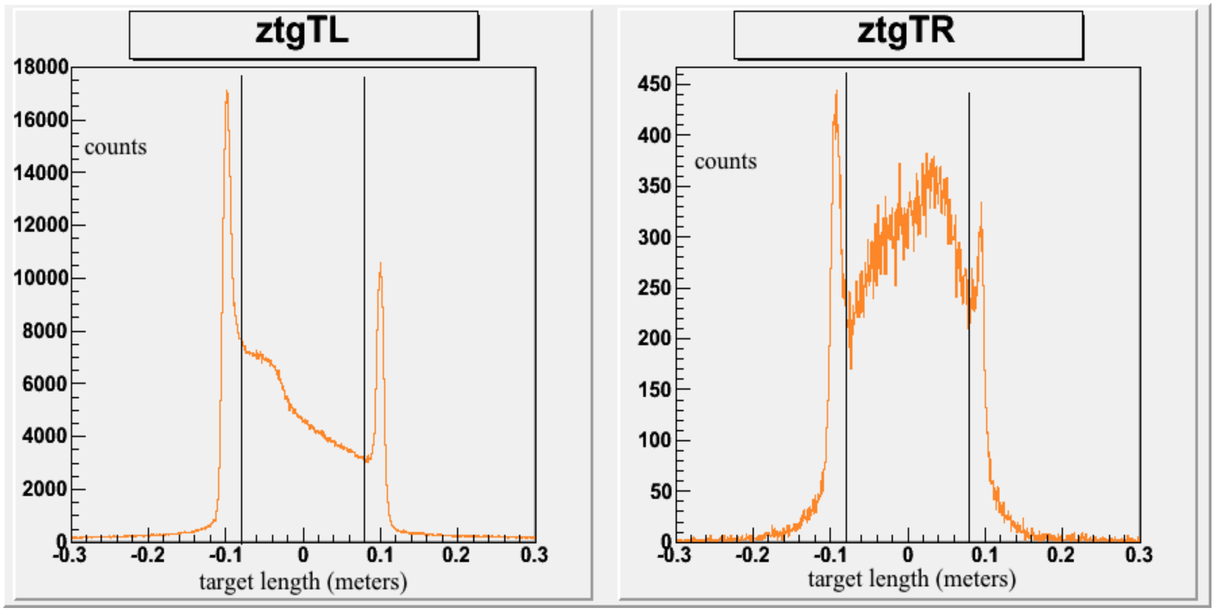

Figure 5.9: 353 MeV/c ztarget cuts placed at +/- 8 cm.

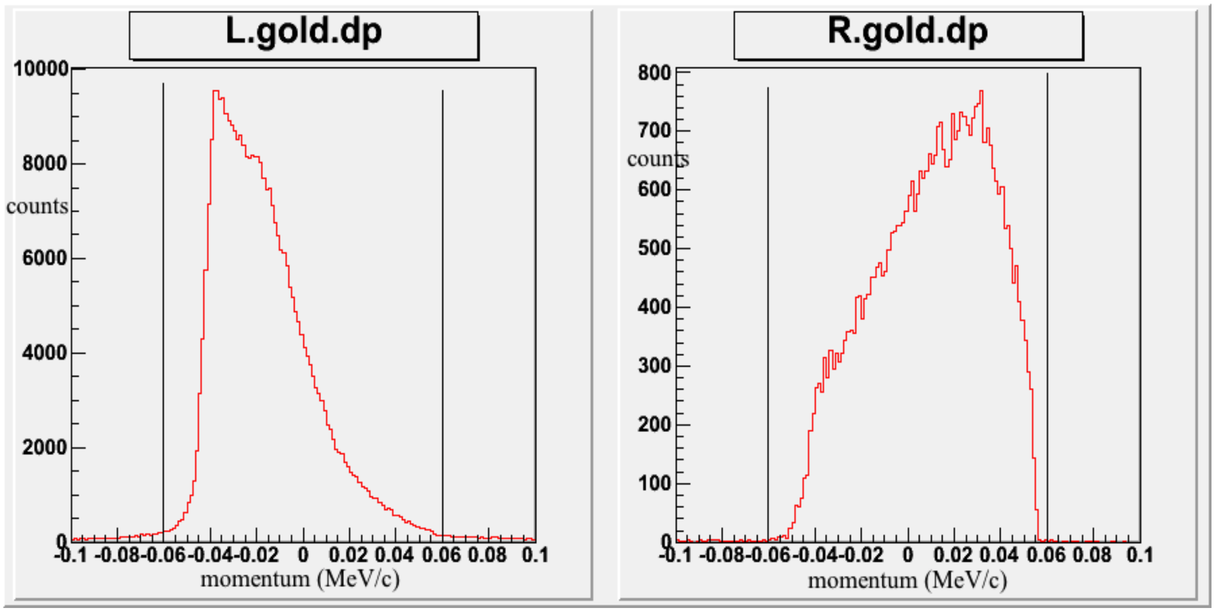

Figure 5.10: 153 MeV/c deviation in central momentum cuts placed at +/- 0.06 MeV/c.

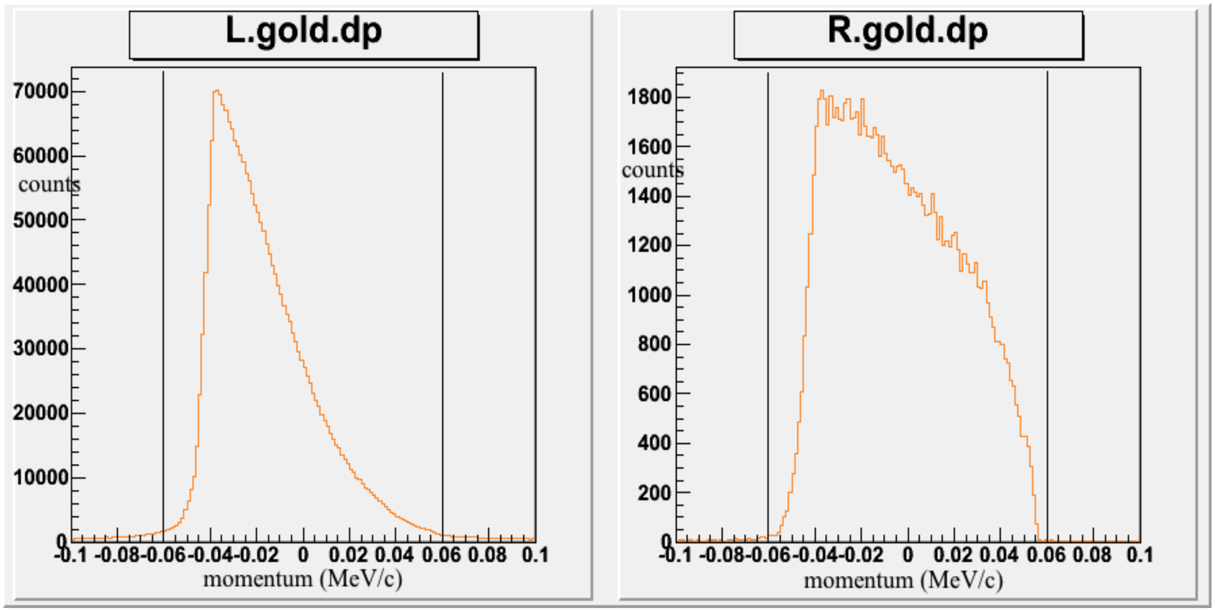

Figure 5.11: 353 MeV/c deviation in central momentum cuts placed at +/- 0.06 MeV/c.

5.2.1 SRC Target Parameters

Typical target parameters for e08009 are shown in table 5.4. A screen shot of the target parameters is shown in figure 5.12.

The SRC target container is an aluminum can of length 20 cm. Cryogenic ^4He enters and exits at the upstream end of the target. There is no outlet for the fluid at the downstream end of the can. A diagram of the target from a computational fluid dynamics (CFD) calculation [3] at 95 μA is shown in figure 5.13. The figure shows that there is a loss of target density from the upstream to the downstream end of the target. In the figure, drho is the loss in percent of density.

5.2.2 Event Distributions Along Beam Axis

The LHRS was held at a fixed angle and a fixed momentum. This allowed us to use the LHRS as a density monitor. An example of the counts/Coulomb is shown in figure 5.14.

There is a decrease in the counting rate from $-0.1m$ to $+0.1m$. This is attributable to two factors. First there is the effect due to the physics of scattering which favors smaller scattering angles. The upstream parts of the target are at smaller angles than the downstream parts with respect to the LHRS. Secondly the CFD calculations predict a decreasing target density from the upstream entry and exit flanges of the fluid to the downstream end cap. This is seen in figure 5.13.

We can treat these two effects as due to a product of two factors. The angular dependence is called $ang(z)$. This is independent of beam current, I. The density effect depends on both the current I, and the position z. The density dependence is

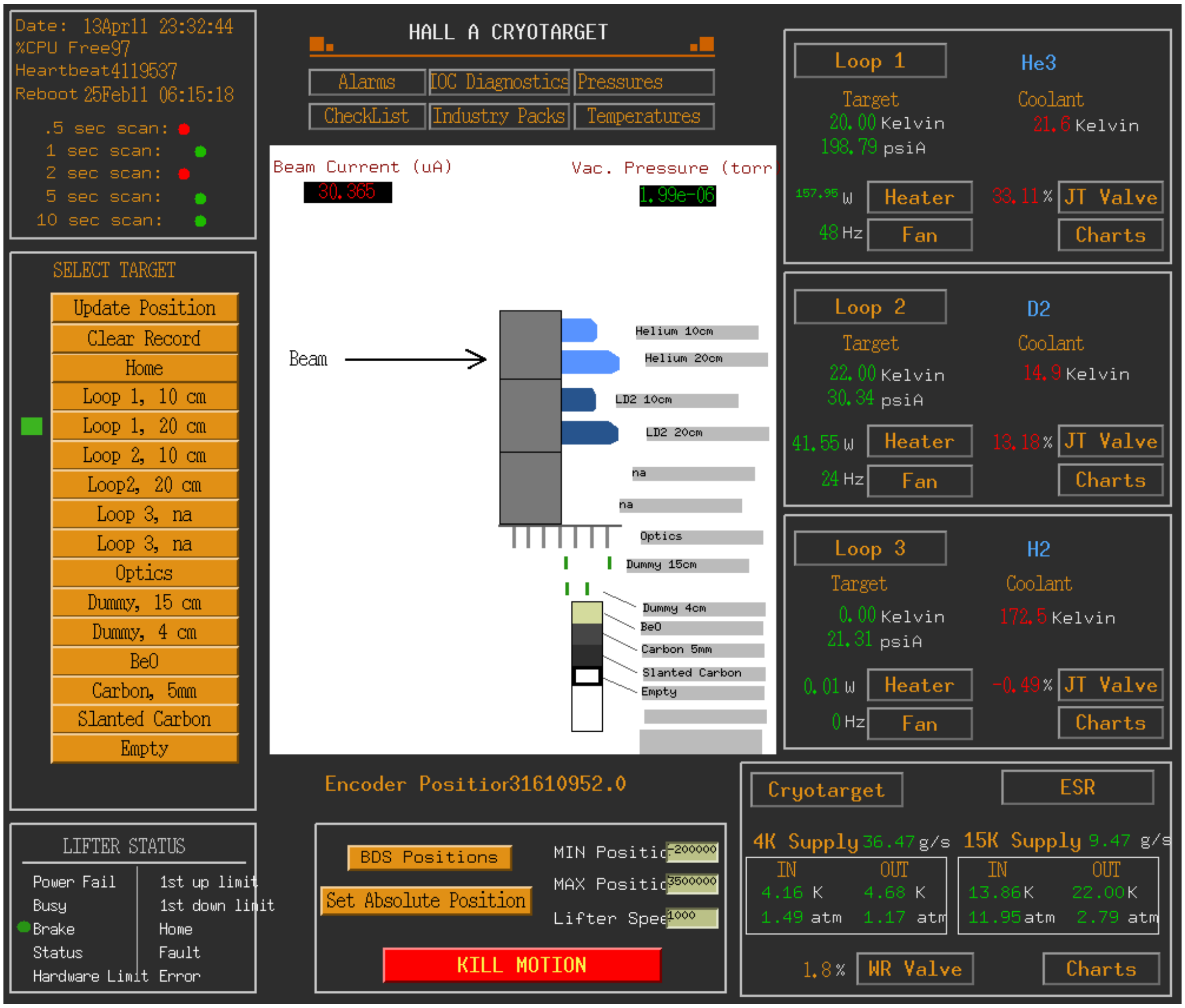

Date: 13Apr11 23:32:44
%CPU Free97
Heartbeat4119537
Reboot 25Feb11 06:15:18
.5 sec scan: ●
1 sec scan: ●
2 sec scan: ●
5 sec scan: ●
10 sec scan: ●

Beam Current (uA) 30.365
Vac. Pressure (torr 1.99e-06

Encoder Positior31610952.0

MIN Positic 200000
MAX Positic 3500000
Lifter Spee 1000

Loop 1 He3
Target 20.00 Kelvin 198.79 psiA
Coolant 21.6 Kelvin
157.95 W Heater
33.11 % JT Valve
48 Hz Fan

Loop 2 D2
Target 22.00 Kelvin 30.34 psiA
Coolant 14.9 Kelvin
41.55 W Heater
13.18 % JT Valve
24 Hz Fan

Loop 3 H2
Target 0.00 Kelvin 21.31 psiA
Coolant 172.5 Kelvin
0.01 W Heater
-0.49 % JT Valve
0 Hz Fan

4K Supply 36.47 g/s
IN 4.16 K 1.49 atm
OUT 4.68 K 1.17 atm

15K Supply 9.47 g/s
IN 13.86K 11.95atm
OUT 22.00K 2.79 atm

1.8 % WR Valve

Figure 5.12: Typical target parameters during E08009. This screen shot shows a beam current of $30\mu A$ with typical target parameters.

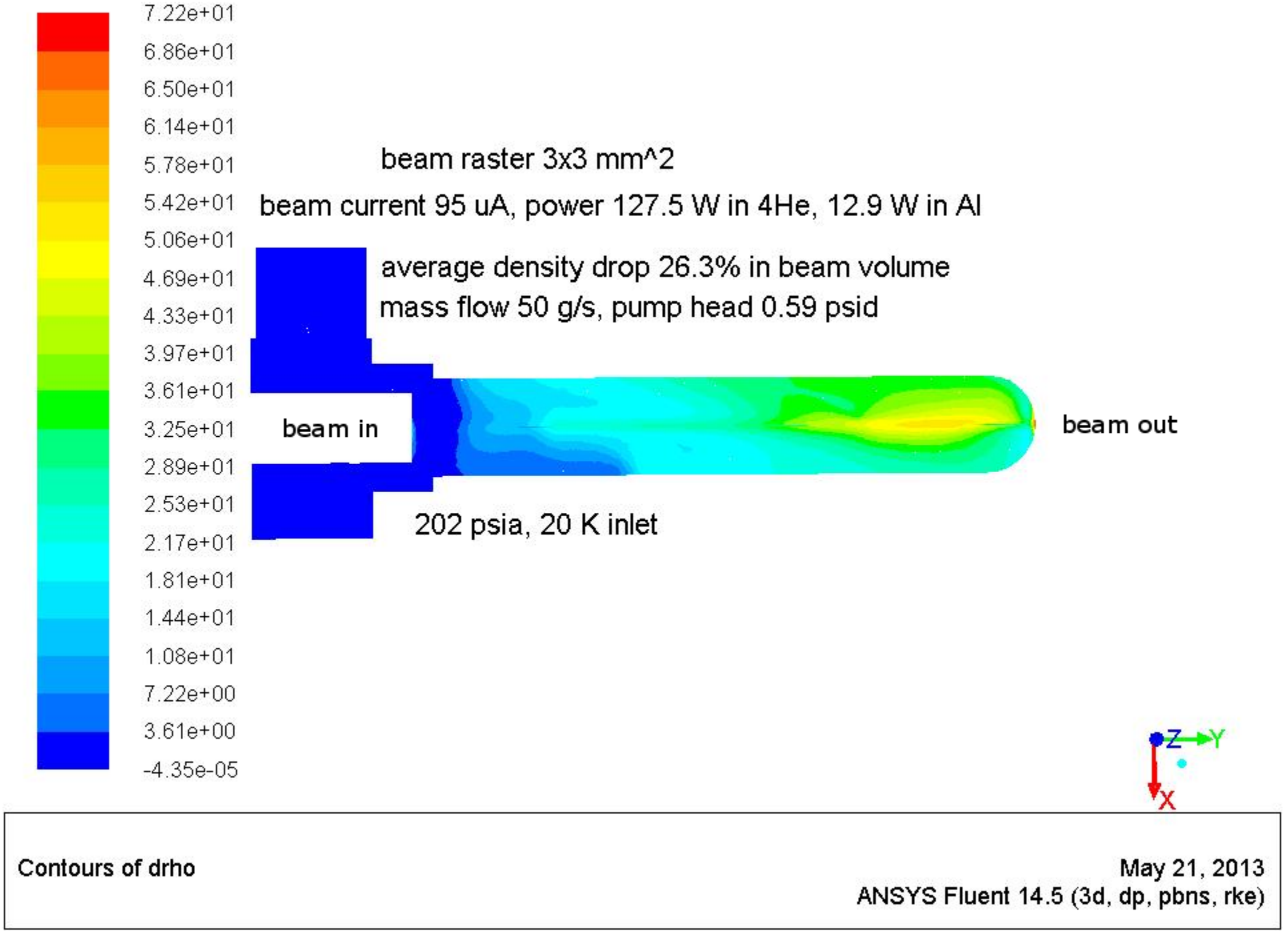

Figure 5.13: Example of a CFD calculation for the SRC target geometry. The beam enters from the left and the cryofluid enters and exits at the flanges at the left. There is no exit for the cryofluid at the right end of the aluminum can. drho is the loss in percent of density. Calculation and image provided by Silviu Covrig [3].

called $den(I, z)$. The rate at point z and for current I is then

$$rate(I, z) \propto ang(z) * den(I, z). \tag{5.1}$$

It is useful to compare the rates at the larger currents to the rate at the smallest current. The ratio of rates is then a measure of the density dependence as a function of position and current.

$$ratio(47\mu A, 4\mu A, z) = \frac{ang(z) * den(47\mu A, z)}{ang(z) * den(4\mu A, z)} = \frac{den(47\mu A, z)}{den(4\mu A, z)}. \tag{5.2}$$

The application of equation 5.2 to a comparison of rates at $47\mu A$ and $60\mu A$ to $4\mu A$ is shown in figure 5.15; the corresponding data file is shown in figure 5.5. The average $\frac{\rho}{\rho_4}$ (from the data file) is multiplied by N_{tgt} in the cross section.

5.2.3 Computational Fluid Dynamic Calculations

An example of the CFD calculation [3] is shown in figure 5.16. The calculations produce a broad band of possible densities for a given value of z. We also have the data file which generates this plot (see table 5.5). Since the experimental results are an average over the densities at any given value of z, we average the CFD data file. A comparison of all three density distributions predicted by CFD is shown in figure 5.17.

We see from figure 5.17 that the CFD calculation for 4 μA shows a small average drop, 2.33% to be exact, from the density calculated solely from temperature and pressure. A factor of 0.9777 +/- 1% is included in the final calculation in column 4 of the experimentally determined density of nuclei (see 5.5 and 5.7).

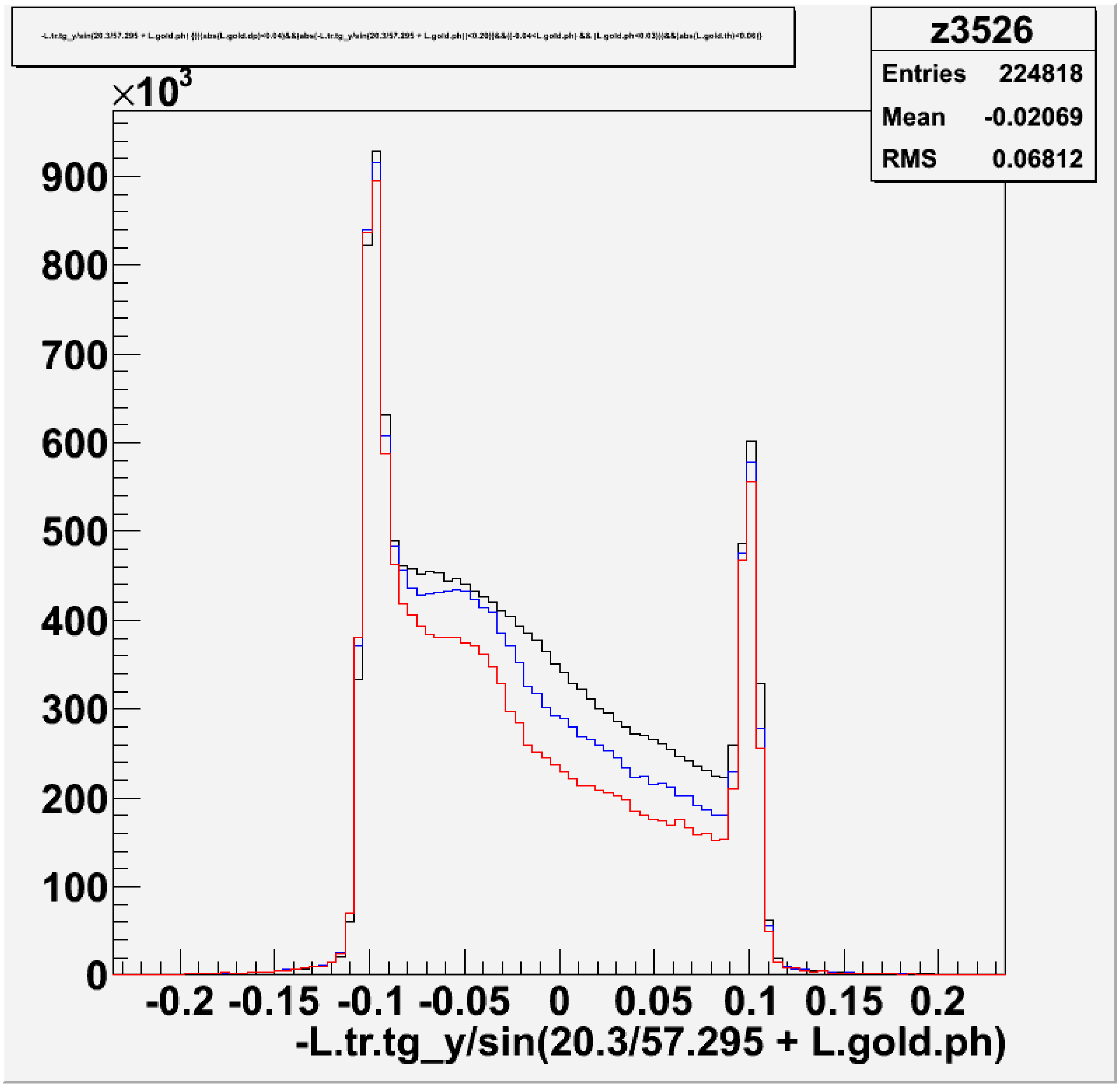

Figure 5.14: Normalized counts per Coulomb(vertical axis) along the beam's path for 4 different beam currents, $4\mu A$(black), $47\mu A$(blue), $60\mu A$(red). The horizontal axis is along z in meters. The aluminum end caps are seen as sharp spikes at ±0.1 m.

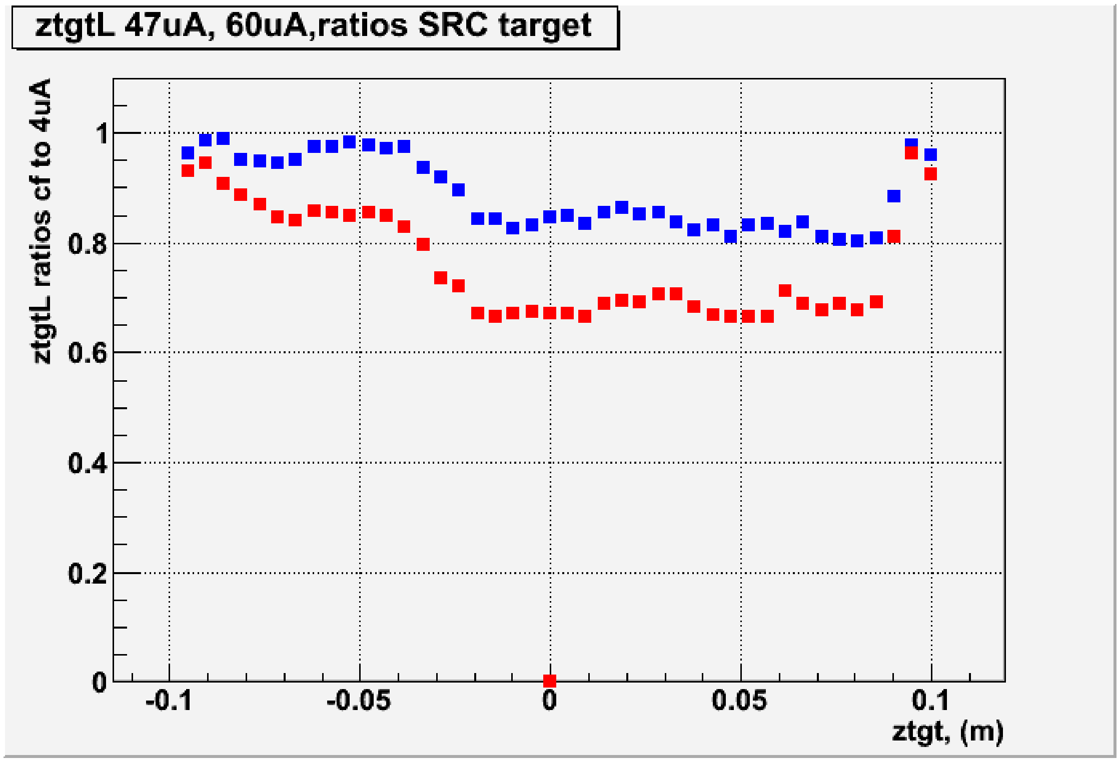

Figure 5.15: Ratio of normalized counts per Coulomb(vertical axis) along the beam's path for 2 different beam currents, versus z position using equation 5.2. The blue squares are for the ratio of $47\mu A$ rate compared to $4\mu A$. The red squares are for the ratio of $60\mu A$ rate compared to $4\mu A$.

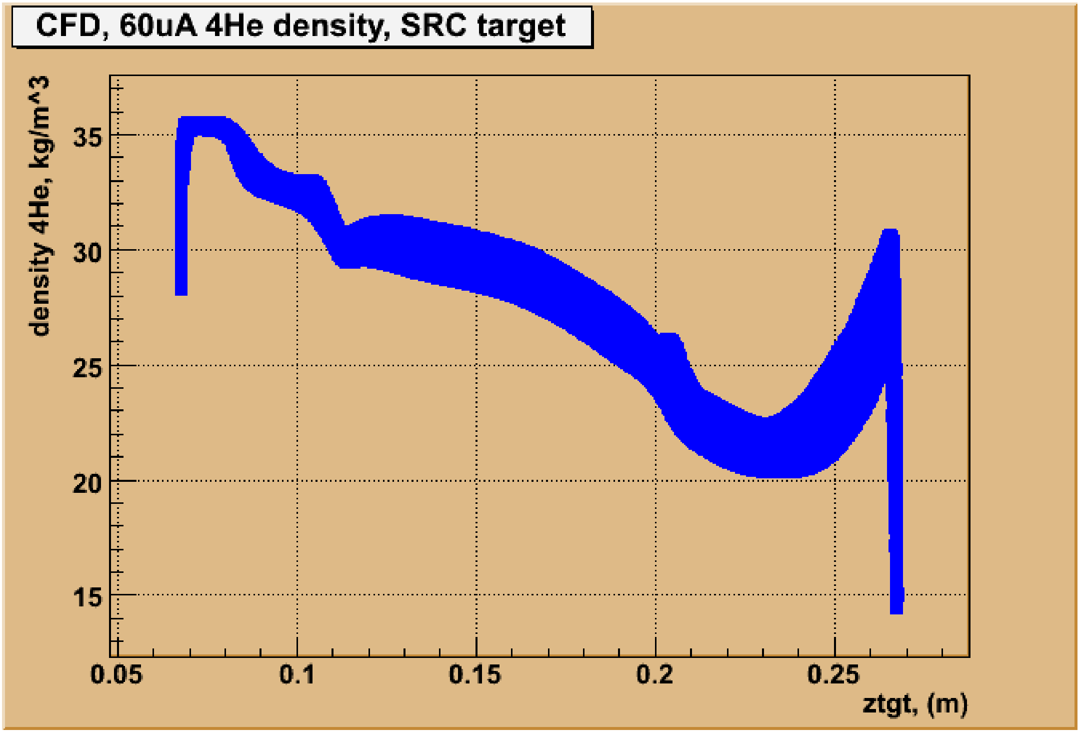

Figure 5.16: Prediction [3] of the changing target density along the beam path for $60\mu A$.

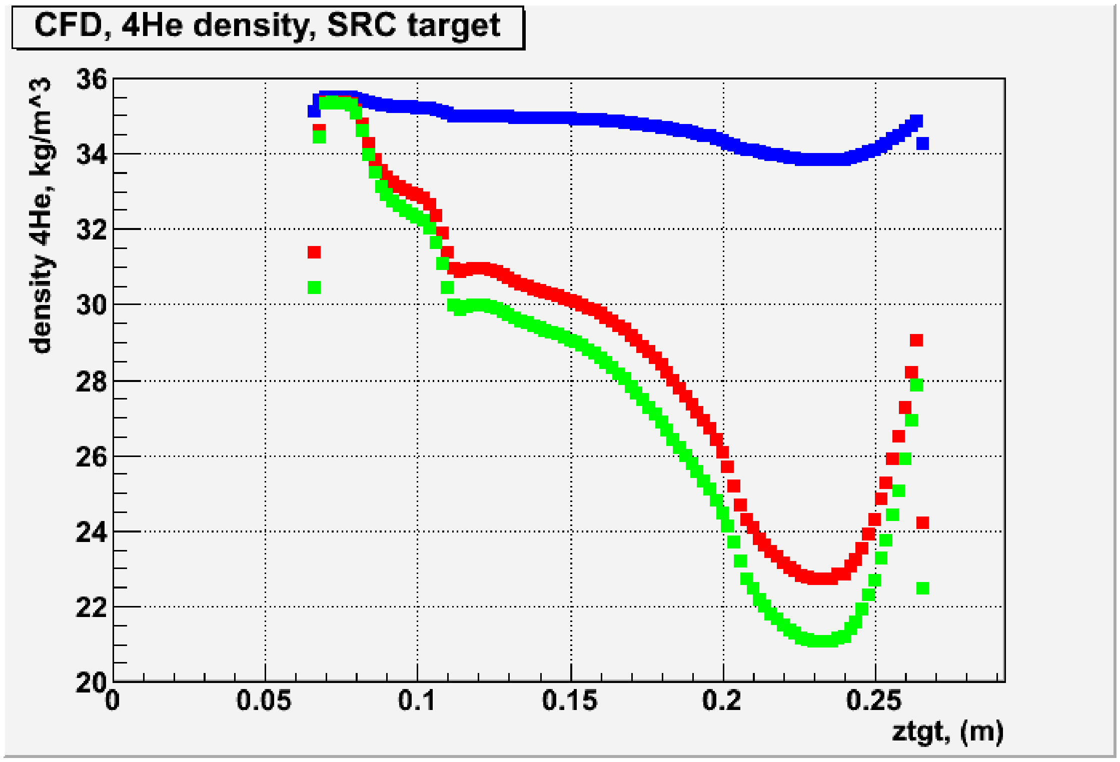

Figure 5.17: Prediction [3] of the changing target density along the beam path for three beam currents, $4\mu A$(blue), $47\mu A$(red), $60\mu A$(green).

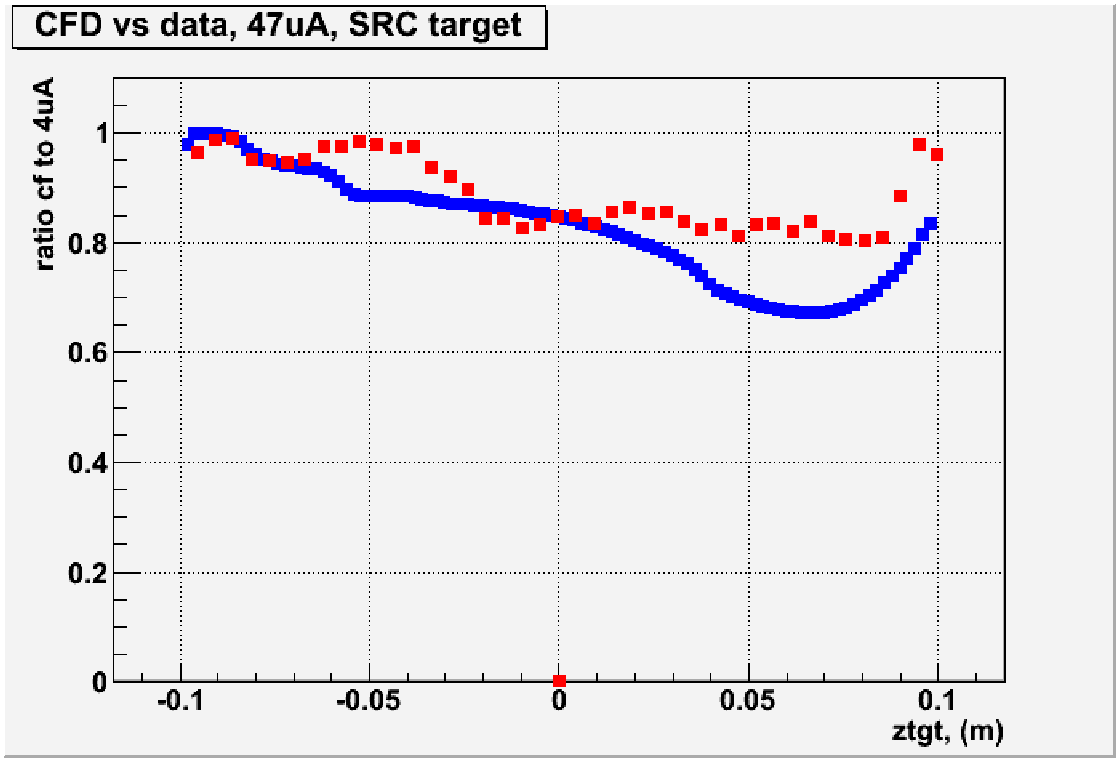

Figure 5.18: Comparison of the ratio of $\frac{den(z,47\mu A)}{den(z,4\mu A)}$ for the data(red) to the CFD(blue) prediction [3] for $47\mu A$.

5.2.4 Comparison of Experimental Count Rate Ratios to CFD

It is possible to check the CFD calculations for the ratios of densities against the data. In figures 5.18 and 5.19 we compare the data and CFD calculations for $47\mu A$ and $60\mu A$.

This is a rather stringent test of the extent to which the CFD code is reliable. In the SRC target the fluid flow is strongly constrained by the closed end downstream cap. The power absorbed by the ^4He cryofluid is also very large. The use of CFD is an important tool for the design of high power cryogenic targets. The target envisioned for the Moller experiment is an example of such a target.

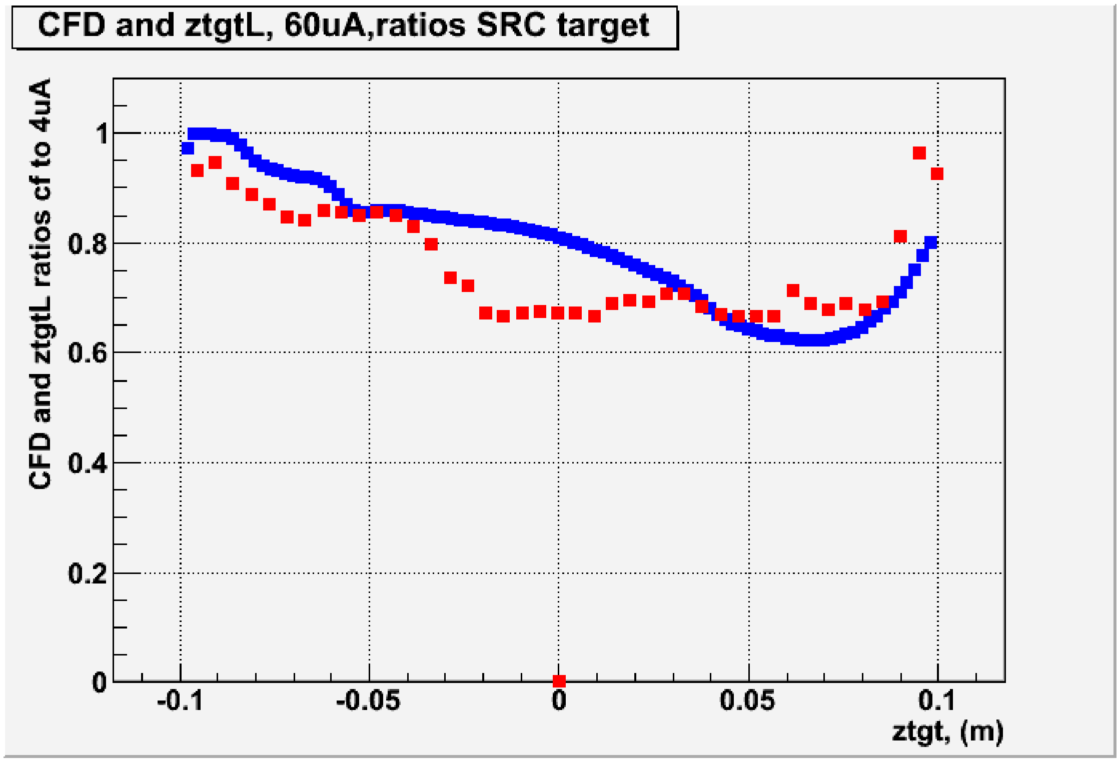

Figure 5.19: Comparison of the ratio of $\frac{den(z,60\mu A)}{den(z,4\mu A)}$ for the data(red) to the CFD(blue) prediction [3] for $60\mu A$.

5.3 Data Corrections for Emiss

The Emiss value from the Hall A analyzer which made the root files does not give the best resolution (see figure 5.20). The Emiss resolution is improved by correcting for the slope of emiss vs. ytarget (see figure 5.21).

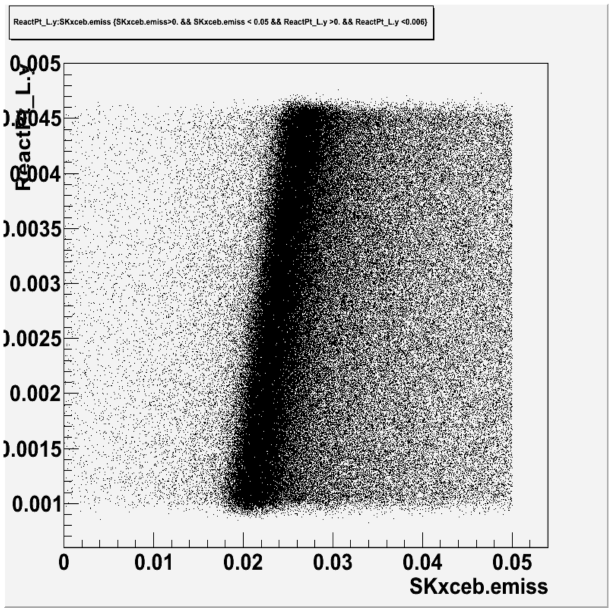

Figure 5.20: Emiss (GeV, x-axis) vs. Ytarget (y-axis) before slope correction.

5.4 GEANT Simulations

GEANT Monte Carlo simulations were performed for the E08009 experiment at Jefferson Lab. The fortran version of GEANT (3.2), packaged as COMGEANT from Eugene Chudakov [4], was used. The simulation provides a missing energy spectrum for the triton ground state from $^4He(e, e'p)^3H$ which is broadened to fit the measured spectrum shape. We also use the simulation to calculate the missing momentum acceptance fraction for 0.05 GeV/c size bins of missing momentum. A calculation of the average cross section from the theoretical cross sections provided by the Madrid

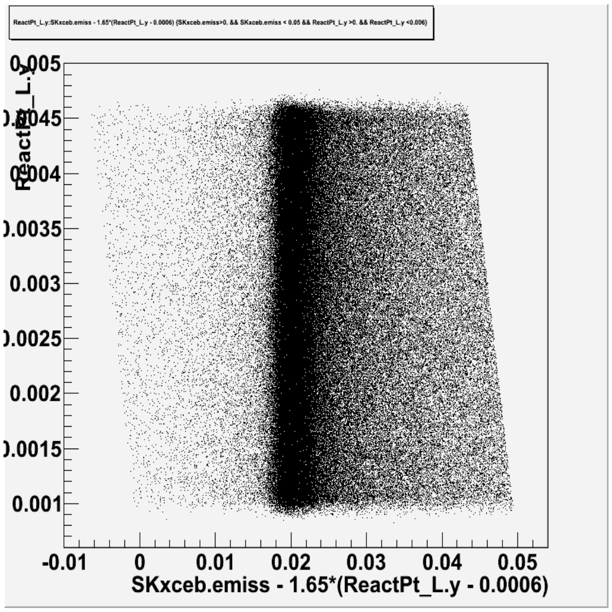

Figure 5.21: Emiss (GeV, x-axis) vs. Ytarget (y-axis) after slope correction.

group [5] for ${}^4He(e,e'p)^3H$ using the simulation is shown.

5.4.1 Using the GEANT3.2/COMGEANT Code

E08009 used a cryogenic target of ${}^4He$ of length 20 cm and $20^\circ K$, 198 psia. Aluminum end caps at the beam in and beam out ends of the target are 20 cm apart. A picture of the target shown with the Computational Fluid Dynamics (CFD) calculation is in figure 5.13. A description of the target's performance is given in reference [6]. In this report we are concerned with the GEANT simulations.

The user portions of the code were written by K. Aniol and employed for the lead/bismuth experiment (E06007) and other experiments requiring a vertex production of a scattered electron and an outgoing particle, h. The type of reaction that can be handled is A(e,e'h)B. The input file contains the massess of A, B, e, and h. The distances, locations and sizes of the apertures to the high resolution spectrometers (LHRS,RHRS) are included. The incident beam energy and central momenta of the HRSs are included. The geometry file includes the target description and all the material between the target and the entrance apertures of the HRSs. Particles are not followed through the spectrometers themselves. Practice has shown that one normally needs to smear the resolutions predicted by Monte Carlo codes even if the spectrometer fields and detector geometries and resolutions are part of the simulation.

The code output is a hbook file containing a ntuple. This hbook file can be analyzed using the CERN paw program or it is converted to a root file for the CERN root program. For each event where a vertex in the target is created the following variables are in the ntuple or root tree for A(e,e'p)B. Coordinates are the Hall A coordinates, z is toward the beam dump, y is vertically upward and x is to the beam left for a RH coordinate system.

`variables from geant:`

`px0,py0,pz0 : incident electron momenta at vertex`

`ee,eex,eey,eev : electron momenta entering LHRS`

`eev,eexv,eeyv,eezv : scattered electron at the vertex`

`xe7,ye7,ze7 : coordinates at entrance of electron to LHRS`

`pproton,ppx,ppy,ppz : proton momenta entering RHRS`

`ppv,ppxv,ppyv,ppzv : proton momenta at the vertex`

`xp8,yp8,zp8 : coordinates at entrance of proton to RHRS`

`xvert,yvert,zvert : coordinates of the vertex`

`xrast0,yrast0 : raster coordinates`

The electron momenta at the vertex, px0, py0, pz0, include external bremsstrahlung which is automatically a feature of GEANT. At the vertex the electrons must also undergo significant radiation loss. Internal bremsstrahlung is not included in the GEANT code so this is handled by a separate user provided subroutine (see appendix). In the cases discussed here this is done by using the Schwinger prescription. The electrons and protons created at the vertex are followed through all remaining material and air to the spectrometer entrances. Additional radiative losses and mulitple scattering are handled by GEANT. Since the vertex kinematical variables are known it is possible to use the GEANT output to weight each vertex with a theoretical cross section. A flow diagram of the GEANT simulation is shown in figure 5.22.

5.4.2 Simulation Results for E08009

The simulation uses the kinematical settings for E08009 listed in table 5.1. The hbook files created by GEANT3.2 are converted to root trees. A separate c++ script called by root generates histograms from the GEANT variables in the root tree.

5.4.3 Missing Momentum Acceptance

The wide momentum acceptance of the the HRSs' allows for a broad missing momentum acceptance. In the simulation each point within the spectrometers' apertures has an equal probability of being a target for a vertex electron and proton. The 3 body kinematical and geometrical limitations for particles arriving at the target points in the apertures are correctly calculated by GEANT. We thus have defined the missing momentum acceptance factor, $f(p_m)$, for a bin of missing momentum centered around p_m as

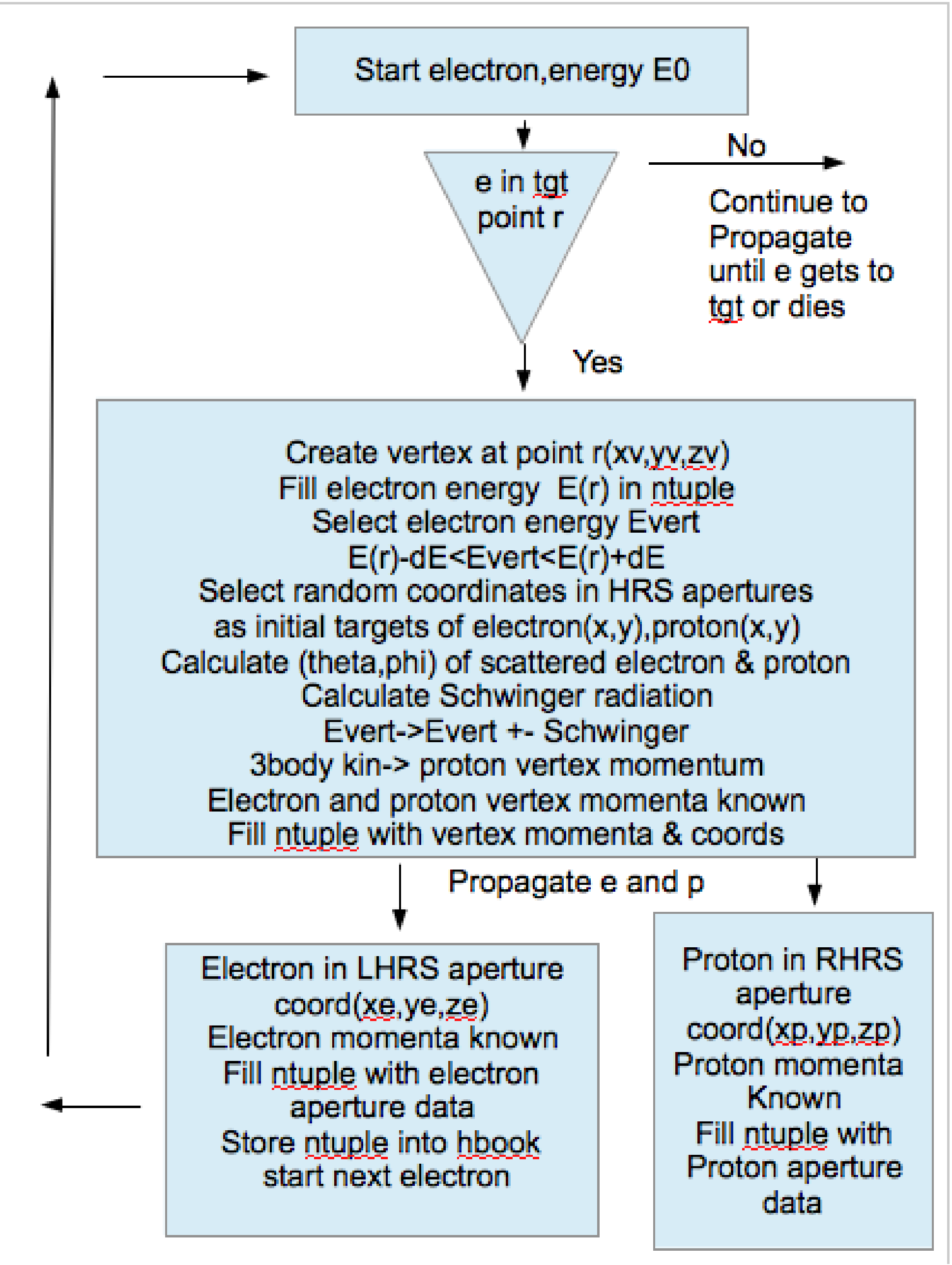

Figure 5.22: The tracking and storage of electrons and protons in the GEANT simulation. The quantity dE = dp*E(r), where dp is typically 0.045 corresponding to the momentum acceptances of the HRSs. Here $E(r) = \sqrt{px0^2 + py0^2 + pz0^2 + m_e^2} - \omega$ is the LHRS central momentum setting.

$$f(p_m) = \frac{n(p_m)}{\sum n(p_m)}. \tag{5.3}$$

Where $n(p_m)$ is the number of triton events in the missing momentum bin centered on p_m and $\sum n(p_m)$ is the total number of triton events over all missing momenta for the particular kinematic setting. An example of GEANT missing momentum spectra binned into 50 MeV/c size bins for the 0.153 GeV/c and 0.353 GeV/c kinematic settings is shown in figure 5.24. The same Gaussian broadening used in figure 5.29 was applied in generating figure 5.24. Table 5.2 lists the simulated fractional acceptance from equation 5.3 for the 0.153 GeV/c and 0.353 GeV/c kinematic settings.

5.4.4 Theoretical Cross Sections From Madrid

Theoretical cross sections [5] were made available in tabular form in terms of the missing momenta and the angle ϕ between the electron scattering plane and the plane formed from the three momentum transfer, $\vec{q}$ and the proton momentum $\vec{p}$. The cross sections, $x_b = 1.24$, for $^4He(e,e'p)^3H$ were averaged over the missing momentum and angular acceptances at the HRS apertures. The Madrid cross sections for $x_b = 1.24$ were only given above 0.153 GeV/c. In table 7.1 the * indicates that a significant fraction of the missing momentum, p_m, accepted by the spectrometers is below 0.153 GeV/c. The average cross sections for these p_m are only approximate.

$$< \sigma(p_m) >= \frac{\int \frac{d\sigma}{dEd\Omega_e d\Omega_p} d\Omega_e d\Omega_p}{\int d\Omega_e d\Omega_p}. \tag{5.4}$$

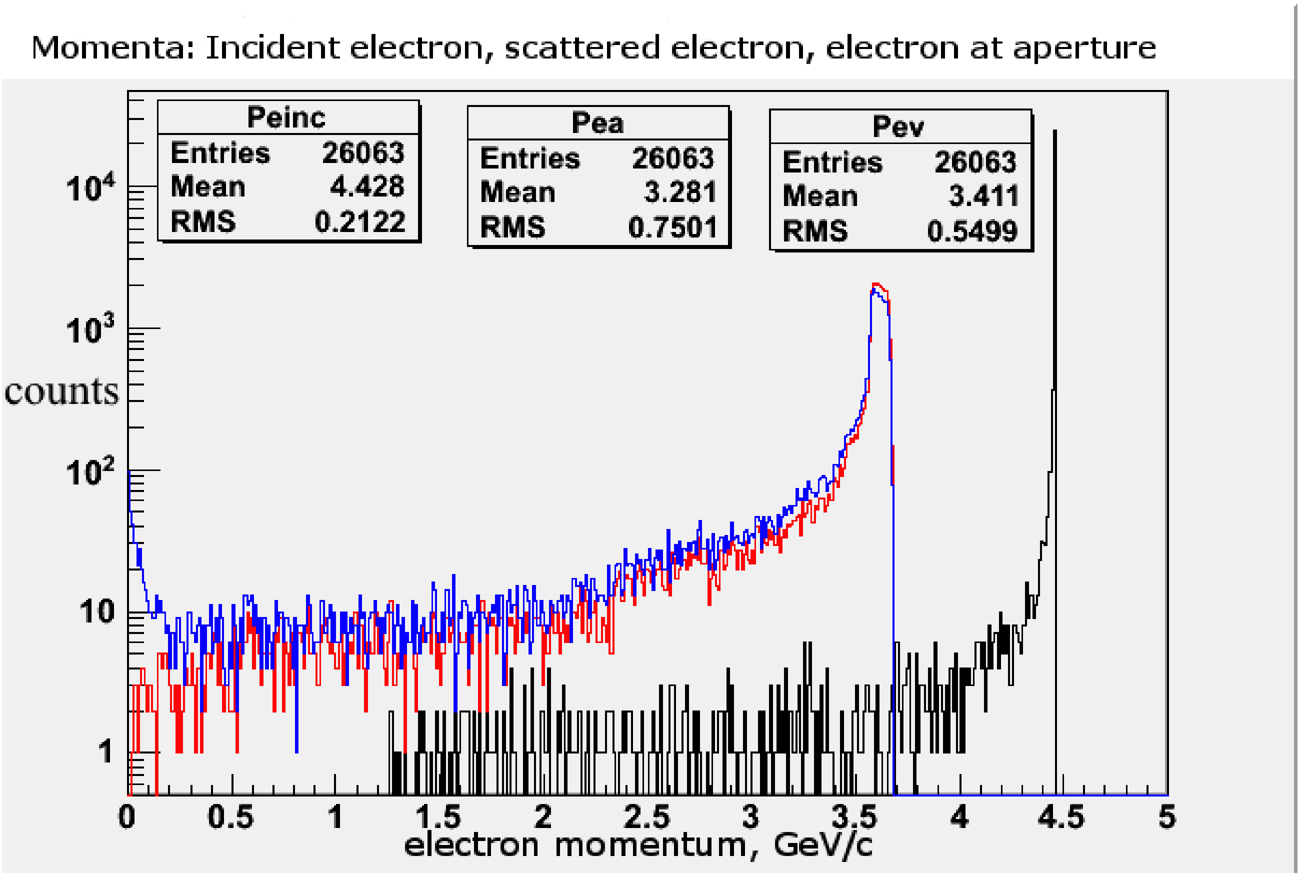

Figure 5.23: Predicted electron momentum spectra for the incident electron at the vertex(black), for the scattered electron at the vertex(red) and for the electron at the aperture(blue). A proton within 4.5% of the RHRS central proton momentum of 1.449 GeV/c is required. The fraction of electrons accepted at the aperture to the electrons leaving the vertex is 0.746.

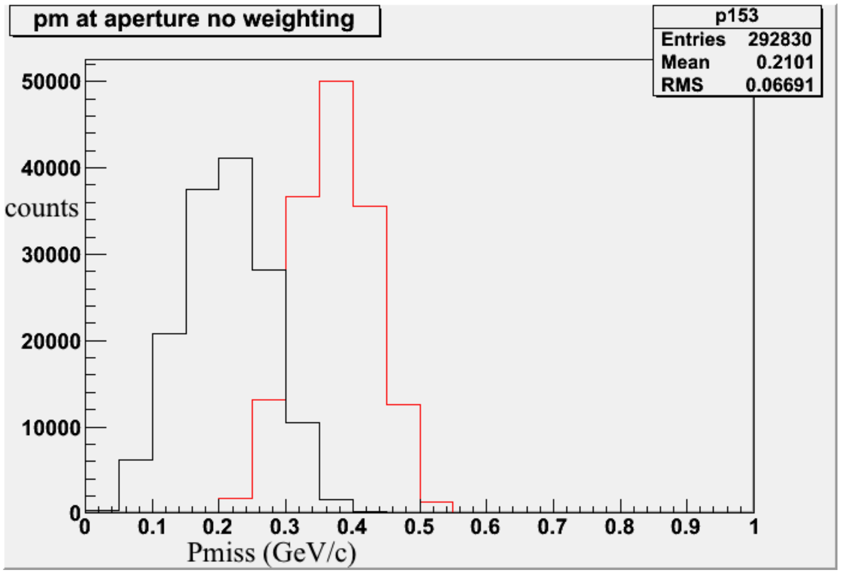

Figure 5.24: GEANT missing momentum spectrum for the 0.153 GeV/c(black) and 0.353 GeV/c(red) kinematic settings based on aperture values. The electron and proton momenta are broadened by the same parameters as in figure 5.29.

5.4.5 Efficiency Correction (ACC(Pm))

The geant simulations show how the geometrical acceptances of the HRSs can be determined for missing momentum bites. The total missing momentum is divided into 50 MeV/c bins. We get the efficiency for capturing a given missing momentum bite by dividing the number of counts in a 50 MeV/c bite by the total number of counts. The plots are shown in figures 5.25 and 5.26. The numerical efficiencies are shown in table 5.8.

5.4.6 Radiative Losses and Multiple Scattering

Examples of losses from the vertex to the aperture are shown in figures 5.23, 5.27 and 5.29 for the electron momentum spectra and the missing energy spectra for the nominal HRS resolution and the broadening and emiss offset needed to fit the data. A

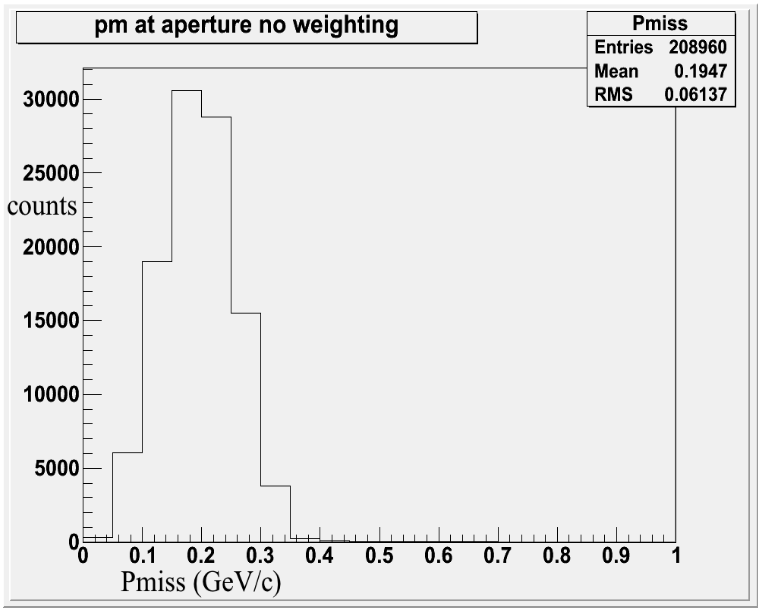

Figure 5.25: 153 MeV/c Pm simulation plot

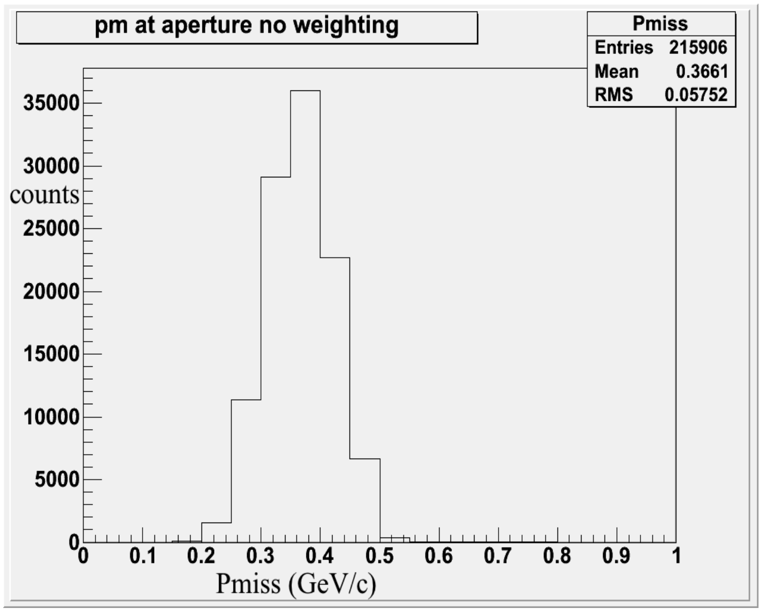

Figure 5.26: 353 MeV/c Pm simulation plot

comparison of the data for 0.153 GeV/c data and simulation is shown in figure 5.29. This comparison enables us to determine the fraction of the triton missing energy spectrum we can use to calculate the cross section. During the root analysis the Gaussian broadening is accomplished on the momenta determined at the apertures via equation 5.5, for example, eex. Here gRandom = new TRandom3(); , mean = 1., and sig1 is varied to fit the width of the data.

$$eex = eex * gRandom.Gaus(mean, sig1); \tag{5.5}$$

5.4.7 Radiative Corrections

After fitting the simulation peak to the data peak at FWHM (see figures 5.27-5.30), a 5 MeV cut is placed around the triton peak. The value of 5 MeV is chosen because it is the same cut placed on the triton peak from the data. The radiative correction can be calculated by the following equation:

$$\frac{\sum_{E_{lo}}^{E_{\infty}}}{\sum_{E_{lo}}^{E_{hi}}}. \tag{5.6}$$

These values are shown in table 5.9. GEANT automatically includes external radiation. Internal radiation is handled by employing the Schwinger prescription.

5.5 Data Tables

.

.

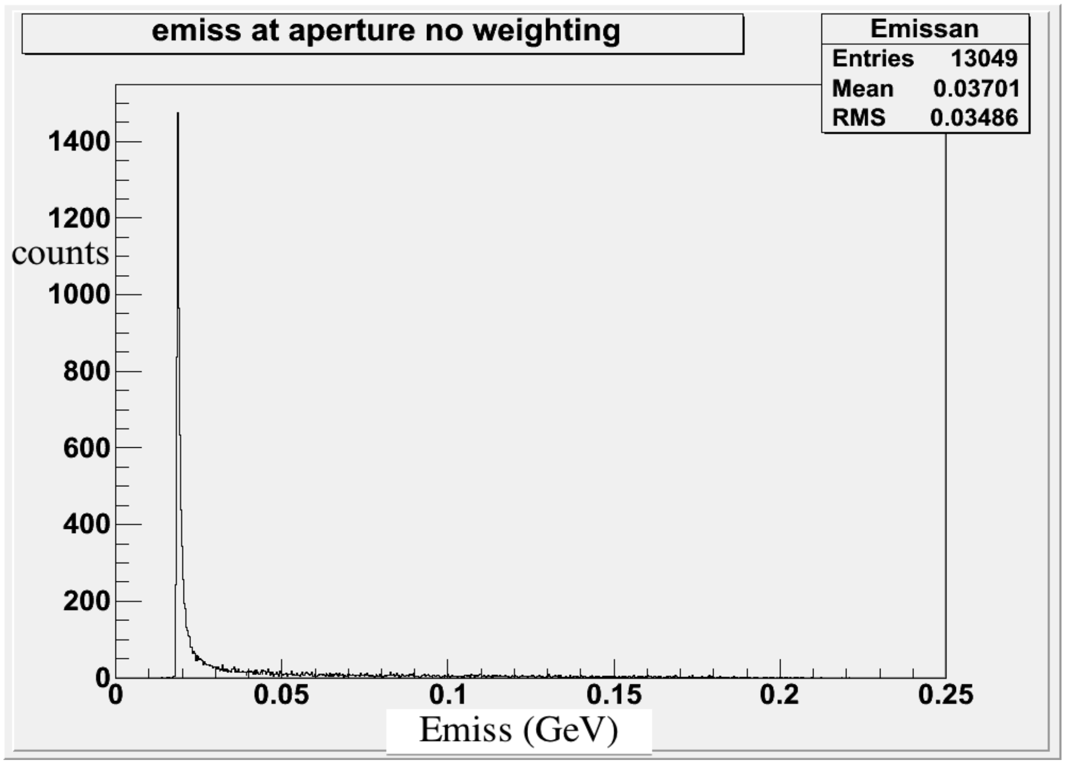

Figure 5.27: GEANT missing energy spectrum for 153 MeV/c simulations before broadening.

Table 5.1: Kinematic settings for E08009. The incident electron energy was 4.4506 GeV, the LHRS was set at 20.3° and 3.601 GeV/c.

P_{miss}	θ_p	RHRS momentum
GeV/c	degrees	GeV/c
0.153	47.0	1.500
0.353	38.5	1.449
0.500	33.5	1.383
0.625	29.0	1.308
0.755	24.5	1.196

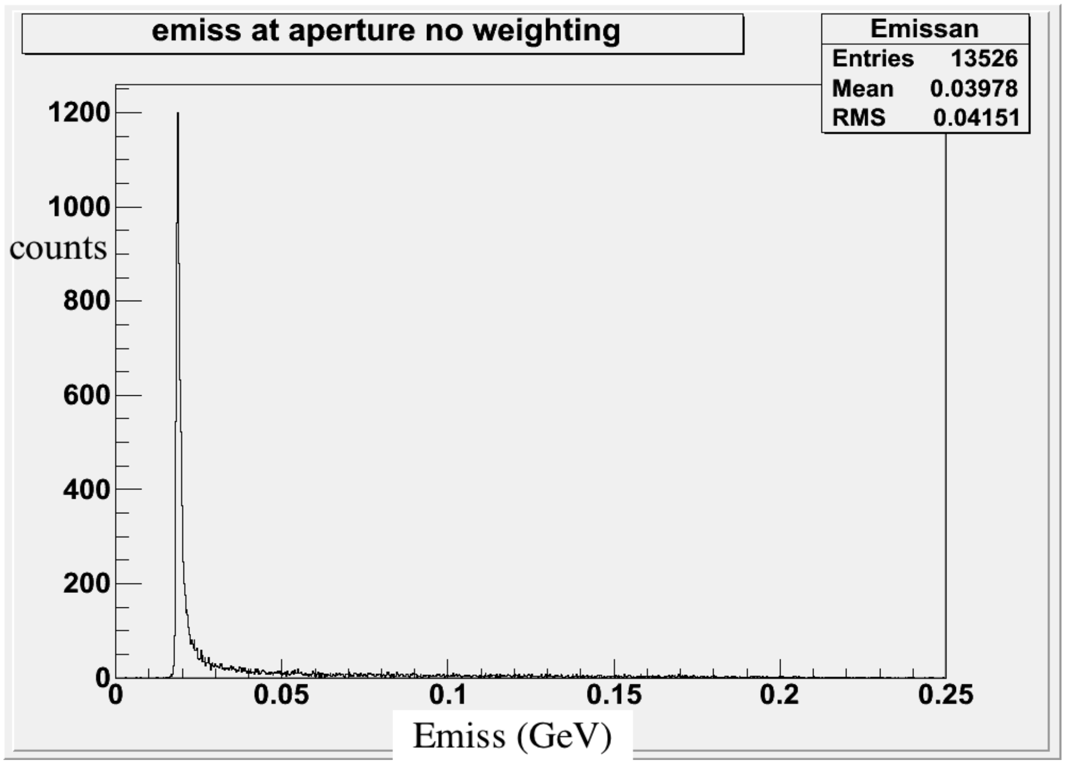

Figure 5.28: GEANT missing energy spectrum for 353 MeV/c simulations before broadening.

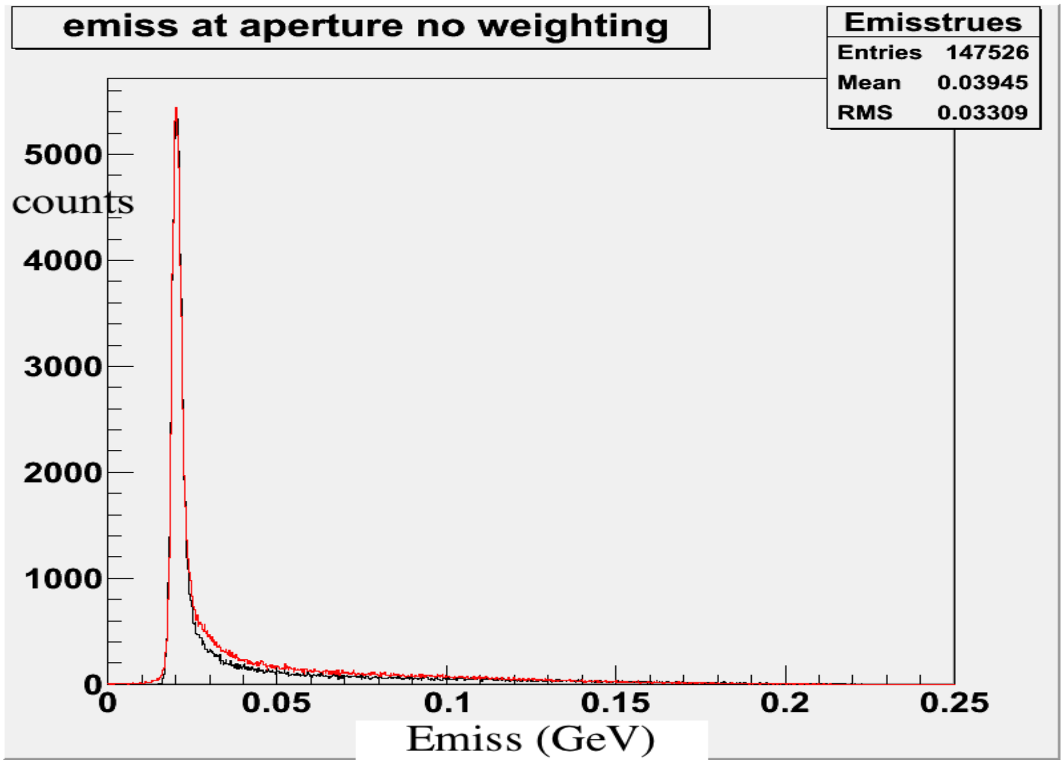

Figure 5.29: GEANT missing energy spectrum for 153 MeV/c simulations after broadening. Data and simulation are overlayed. The darker color represents the simulation while the lighter color represents the data.

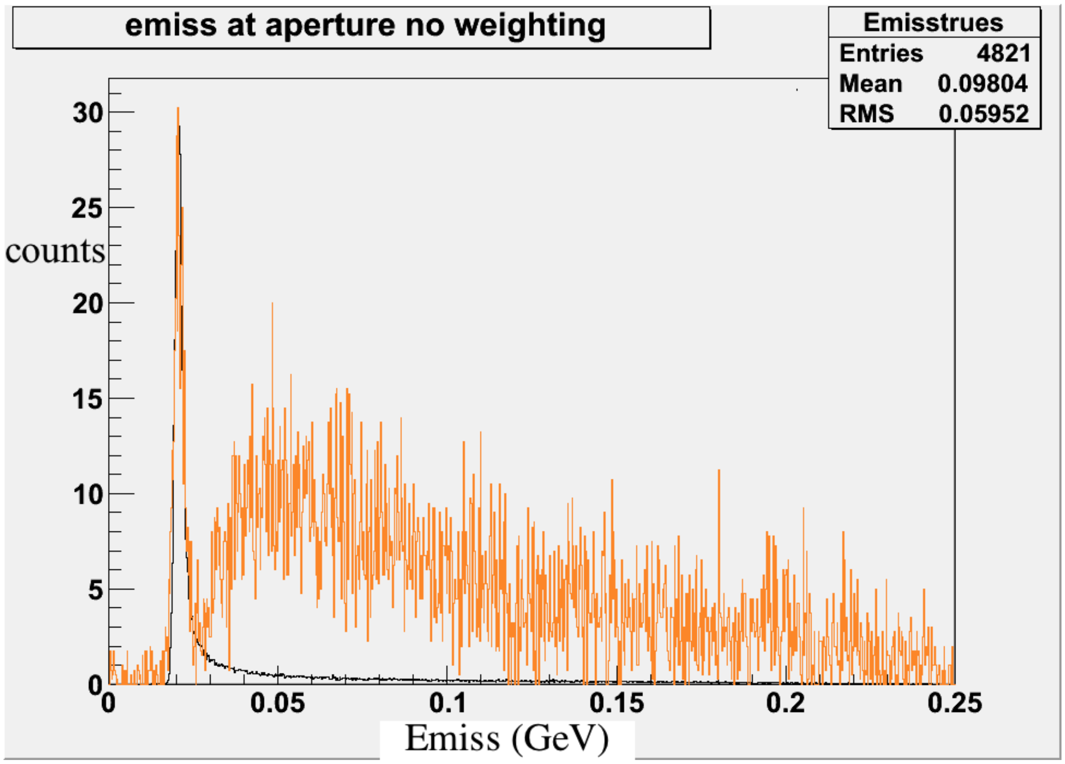

Figure 5.30: GEANT missing energy spectrum for 353 MeV/c simulations after broadening. Data and simulation are overlayed. The darker color represents the simulation while the lighter color represents the data.

Table 5.2: Missing momentum fractional acceptance at the apertures from the simulation. The fraction, $f(p_m)$, is calculated from equation 5.3 using data from the 0.153 GeV/c and 0.353 GeV/c kinematic settings shown in figure 5.24-5.26.

p_m bin	$f(p_m)$	$\delta f(p_m)$	$f(p_m)$	$\delta f(p_m)$
GeV/c	for 0.153	for 0.153	for 0.353	for 0.353
0.0-0.05	0.0021	0.00012		
0.05-0.10	0.0421	0.00054		
0.10-0.15	0.1423	0.00099		
0.15-0.20	0.2558	0.00132	0.00065	0.00007
0.20-0.25	0.2808	0.00138	0.01128	0.0003
0.25-0.30	0.1927	0.00115	0.08666	0.0008
0.30-0.35	0.0713	0.00070	0.24192	0.0013
0.35-0.40	0.0108	0.00027	0.33097	0.0015
0.40-0.45	0.0011	0.00009	0.23523	0.0013
0.45-0.50	0.0004	0.00006	0.08335	0.0007
0.50-0.55			0.00889	0.00024
0.55-0.60			0.00044	0.00005
0.60-0.65			0.00022	0.00004
0.65-0.70			0.00015	0.00003

Table 5.3: Cuts

parameters	value for left or right spectrometers
horizontal angle θ	+/- 0.04 radians
vertical angle ϕ	+/- 0.03 radians
ztarget	+/- 8 cm.
deviation in central momentum	+/- 0.06 MeV/c

Table 5.4: Target Parameters

^4He pressure	199 psia
Temperature	20.0 Kelvin

Table 5.5: Beam heating correction (data values that generate figure 5.15, ρ_4 refers to density for $4\mu A$)

ztgtL	$\frac{\rho}{\rho_4}$ 47 μA	ztgtL	$\frac{\rho}{\rho_4}$ 60 μA
-0.0763	0.943052	-0.0763	0.865422
-0.07154	0.93729	-0.07154	0.839678
-0.06678	0.943727	-0.06678	0.834183
-0.06202	0.96667	-0.06202	0.849308
-0.05726	0.96435	-0.05726	0.844171
-0.0525	0.968192	-0.0525	0.838098
-0.04774	0.963218	-0.04774	0.842712
-0.04298	0.958084	-0.04298	0.8368
-0.03822	0.958948	-0.03822	0.817488
-0.03346	0.923571	-0.03346	0.785774
-0.0287	0.904464	-0.0287	0.723651
-0.02394	0.88273	-0.02394	0.709529
-0.01918	0.829263	-0.01918	0.660151
-0.01442	0.828324	-0.01442	0.655591
-0.00966	0.8123	-0.00966	0.659894
-0.0049	0.818258	-0.0049	0.663071
-0.00014	0.831077	-0.00014	0.658057
0.00462	0.833656	0.00462	0.658626
0.00938	0.818224	0.00938	0.650441
0.01414	0.834197	0.01414	0.672255
0.0189	0.841216	0.0189	0.678293
0.02366	0.829527	0.02366	0.674183
0.02842	0.831924	0.02842	0.686636
0.03318	0.81025	0.03318	0.684254
0.03794	0.794173	0.03794	0.660563
0.0427	0.799589	0.0427	0.64239
0.04746	0.777434	0.04746	0.638631
0.05222	0.795437	0.05222	0.637336
0.05698	0.797928	0.05698	0.634274
0.06174	0.782222	0.06174	0.67827
0.0665	0.7993	0.0665	0.657787
0.07126	0.773588	0.07126	0.644152
0.07602	0.770084	0.07602	0.658396
Average	0.8582505152	Average	0.7163656061

Table 5.6: CFD correction (data values that generate figures 5.17)

^{4}He density $^{4}\mu A$ average	average density divided by maximum value 35.4672	uncertainty
34.68	0.9777	0.01115

Table 5.7: Density Calculation (Average Ntgt calculated from beam heating correction and CFD correction)

Beam current (μA)	Density (nuclei/cm^3) from temperature and pressure	Ntgt (nuclei/cm^2) for +/- 8 cm.	Average Ntgt (nuclei/cm^2) in beam
45.46	5.014×10^{21}	8.023×10^{22}	6.732E$\times10^{22}$
60.71	5.053×10^{21}	8.084×10^{22}	5.662×10^{22}

Table 5.8: ACC(Pm)

channels (MeV/c)	153 MeV/c Efficiency (ACC(Pm))	353 MeV/c Efficiency (ACC(Pm))
0-50	0.0028619287	
50-100	0.0579181622	
100-150	0.1820244078	
150-200	0.2928164633	
200-250	0.2758171811	0.0144425402
250-300	0.1482364202	0.1052758349
300-350		0.2697299551
350-400		0.333456853
400-450		0.2101533188

Table 5.9: Radiative Corrections

	153 MeV/c	353 MeV/c
Number of counts between 18-250 MeV	126342.5	574.18
Number of counts in 18-23 MeV	72249.8	327.7065
Radiative Correction	1.74869	1.75212

CHAPTER 6

Calculation of Cross Section

6.1 Extraction of the 4He(e,e'p)3H Cross Section

The goal is to measure the average cross section per missing momentum bin. This is given by

$$< \sigma(p_m) >= \frac{n(p_m) * RC}{\Delta\Omega_e \Delta\Omega_p \Delta E_e N_e N_{tgt} * EFF}. \tag{6.1}$$

- $< \sigma(p_m) >= \frac{d^5\sigma}{d\Omega_e d\Omega_p dE_e}$ is the average cross section for every 50 MeV/c p_m bin. This result is shown at the start of chapter 7.
- $n(p_m)$ is the net counts in the triton peak after the randoms and background have been subtracted. Refer to tables 6.4 and 6.5. A description of the background subtraction is explained in figures 6.1-6.3.
- RC is the radiative correction to account for the radiative tail that is outside our missing energy cut. Refer to table 5.9.
- $\Delta\Omega_e$ and $\Delta\Omega_p$ are the geometrical solid angles used by the spectrometer apertures. Refer to figure 5.4 on page 35 as an example. Both $\Delta\Omega_e$ and $\Delta\Omega_p$ are calculated by the following equation: 2×0.04 radians $\times\ 2 \times 0.05$ radians $=$ 0.008 steradians.
- ΔE_e is the size of the electron's momentum bin in coincidence with the protons; it is the proton arm that determines ΔE_e. The RHRS dipole momentum is

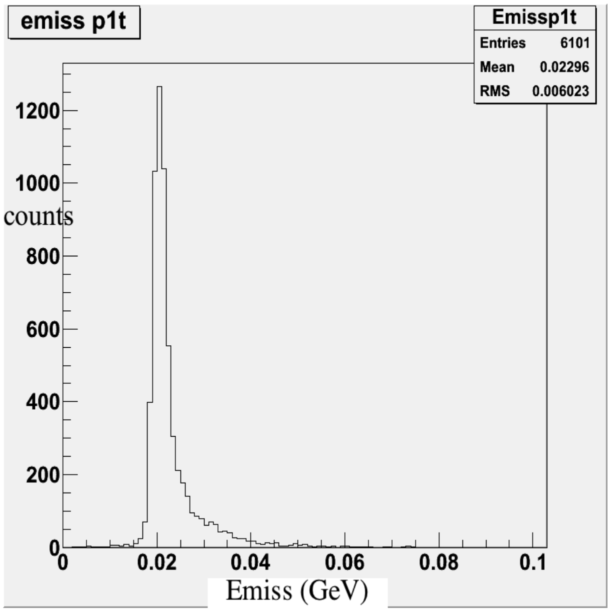

Figure 6.1: 153 MeV Emiss plot with a Pmiss cut of 0-50 MeV/c, before any background subtraction.

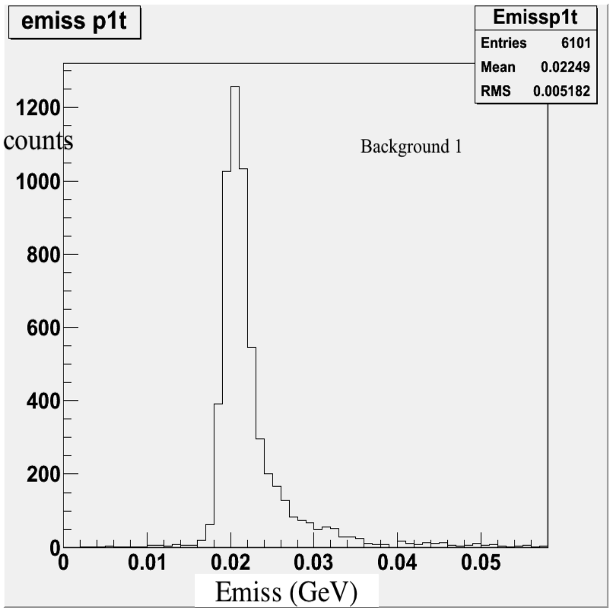

Figure 6.2: 153 MeV Emiss plot with a Pmiss cut of 0-50 MeV/c, after a straight line subtraction from 15 MeV to 40 MeV. The net counts (for this Pmiss cut) come from this plot.

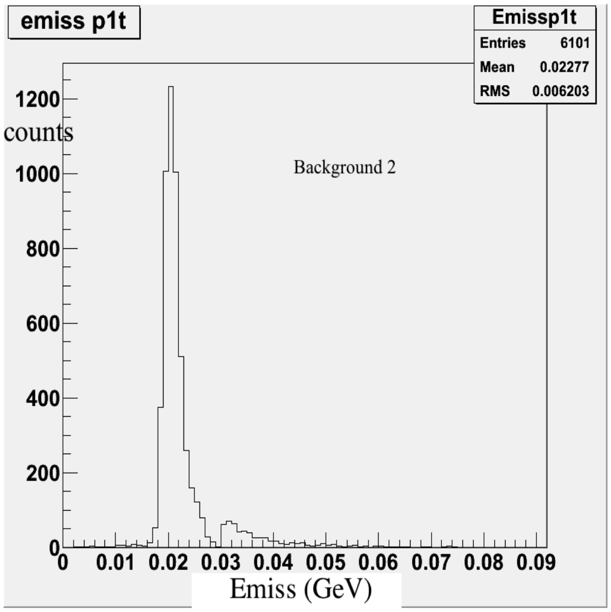

Figure 6.3: 153 MeV Emiss plot with a Pmiss cut of 0-50 MeV/c, after a straight line subtraction from 15 MeV to 30 MeV. This plot is used to calculate ΔBackground.

1.51 GeV/c and 1.449 GeV/c for kinematic values 153 MeV/c and 353 MeV/c respectively. The horizontal markers in figures 6.4 and 6.5 represent +/- 10% of these values. Numerical values are listed in table 6.2.

- $N_e = Q/e$, the number of electrons that passed through the target, where e is the charge on an electron and Q is the total charge. Refer to table 6.3.
- $N_{tgt} = \rho(I) * z_{tgt}$ is the number of nuclei per cm^2 in the beam. I is the beam current, $\rho(I)$ is the number of nuclei per cm^3 and z_{tgt} is the cut on target length. Refer to table 5.7.
  - $\rho(I) = \rho(Temperature, Pressure) * BH(I)$
    - $BH(I)$ is the beam heating effect for current I. Refer to table 5.5 for the data.

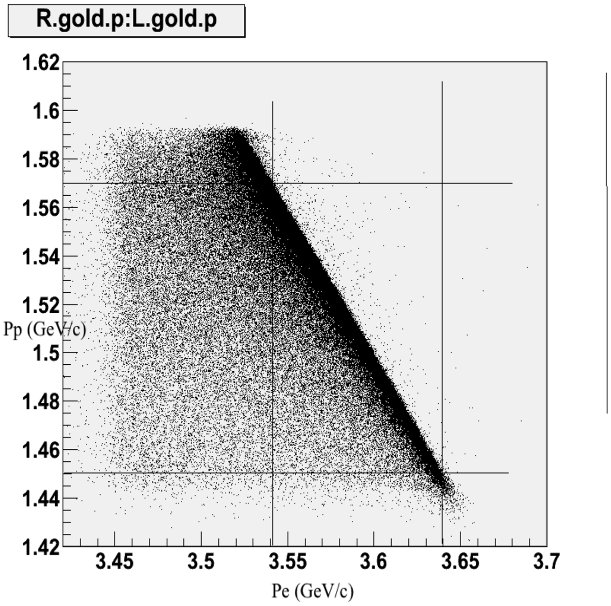

Figure 6.4: 153 MeV/c Proton momentum vs. Electron momentum.

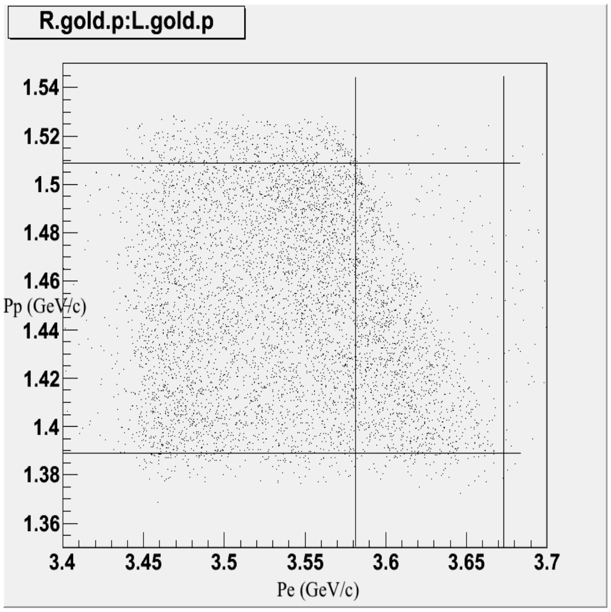

Figure 6.5: 353 MeV/c Proton momentum vs. Electron momentum.

- $EFF = ACC(P_m)$∗LTdaq∗LTelectronics∗trigger efficiency∗wire chamber efficiency∗tracking efficiency. This is the efficiency factor, which is composed of the following terms:
  - $ACC(Pm)$ is the kinematical acceptance of coincidence events for a given missing momentum. Refer to table 5.8.
  - $LTdaq$ is the live time of the triggers acquisition system. Refer to table 6.1.
  - the rest of the effiencies are displayed in table 7.5 and explained in chapter 4.

6.2 Data Analysis Tables

Table 6.1: Average live time of triggers DAQ

153 MeV/c charge (C)	353 MeV/c charge (C)
0.91579	0.94952

Table 6.2: ΔE_e

	x_{lo} (from plot)	x_{hi} (from plot)	ΔE_e
0.153	3.541	3.640	0.0990
0.353	3.582	3.673	0.0915

Table 6.3: N_e

	153 MeV/c charge (C)	353 MeV/c charge (C)
SUM	1.09087	1.74909
number of electrons (Q/e)	6.809E+18	1.092E+19
uncertainty	0.005	0.005

Table 6.4: 153 MeV data for calculating X-section. Δ T = $\sqrt{Trues + 0.25^2 * (T+R)^2}$. Bgd$_1$ is a sloped straight line background from 15-40 MeV. An example is shown in figure 6.2.

Pm cut (GeV/c) in Em	Net counts (T-R-Bgd$_1$) in triton peak	Δ T	True (T) counts in triton peak	Random (R) counts in triton peak
0.0-0.05	4251.05	67.510	4289.25	15
0.05-0.10	28673.93	176.251	29236	76
0.10-0.15	24999.94	164.890	25588.25	79
0.15-0.20	9236.4	100.722	9547.75	29
0.20-0.25	1739.6	44.288	1846	4
0.25-0.30	199.4	15.480	225.5	2

Table 6.5: 353 MeV data for calculating X-section. Δ T = $\sqrt{Trues + 0.25^2 * (T + R)^2}$. Bgd$_1$ is a sloped straight line background from 15-30 MeV. An example for 153 MeV/c is shown in figure 6.2.

Pm cut (GeV/c) in Em	Net counts (T-R-Bgd$_1$) in triton peak	Δ T	True (T) counts in triton peak	Random (R) counts in triton peak
0.20-0.25	36	6.49	41.5	2
0.25-0.30	75.875	9.708	88	20
0.30-0.35	93.45838	9.94	94.75	13
0.35-0.40	67.54162	9.042	78	12
0.40-0.45	17.16662	4.5	19	4

CHAPTER 7

Results and Discussion

7.1 Cross Section Results

The cross section results are presented here. In figure 7.1, the first two theory values (represented with an asterisk) are underestimates because the theory values we have are only valid above 150 MeV/c. However, the 153 MeV/c simulation (represented with a closed dot) continues below 150 MeV/c.

7.2 Uncertainties in the 4He(e,ep)3H Analysis

The total uncertainty is calculated according to the following equation: $\Delta\sigma_{total} =$

$$\sqrt{\Delta\sigma^2_{NetCounts} + \Delta\sigma^2_{Background} + \Delta\sigma^2_{radiativecorrection} + \Delta\sigma^2_{\Delta E} + \Delta\sigma^2_{N_e} + \Delta\sigma^2_{N_{tgt}} + \Delta\sigma^2_{computerdeadtime} + \Delta\sigma^2_{electronicdeadtime} + \Delta\sigma^2_{triggerefficiency} + \Delta\sigma^2_{wirechamberefficiency} + \Delta\sigma^2_{trackingefficiency}}. \tag{7.1}$$

Each component is calculated according to the following formula: $\Delta\sigma_{Parameter} = \sigma\frac{\Delta Parameter}{Parameter}$, except for $\Delta\sigma_{Background}$, which is calculated as $\sigma\frac{\Delta Background}{Netcounts}$. These uncertainties are shown in tables 7.3, 7.4 and 7.5.

7.3 Tabulated Results

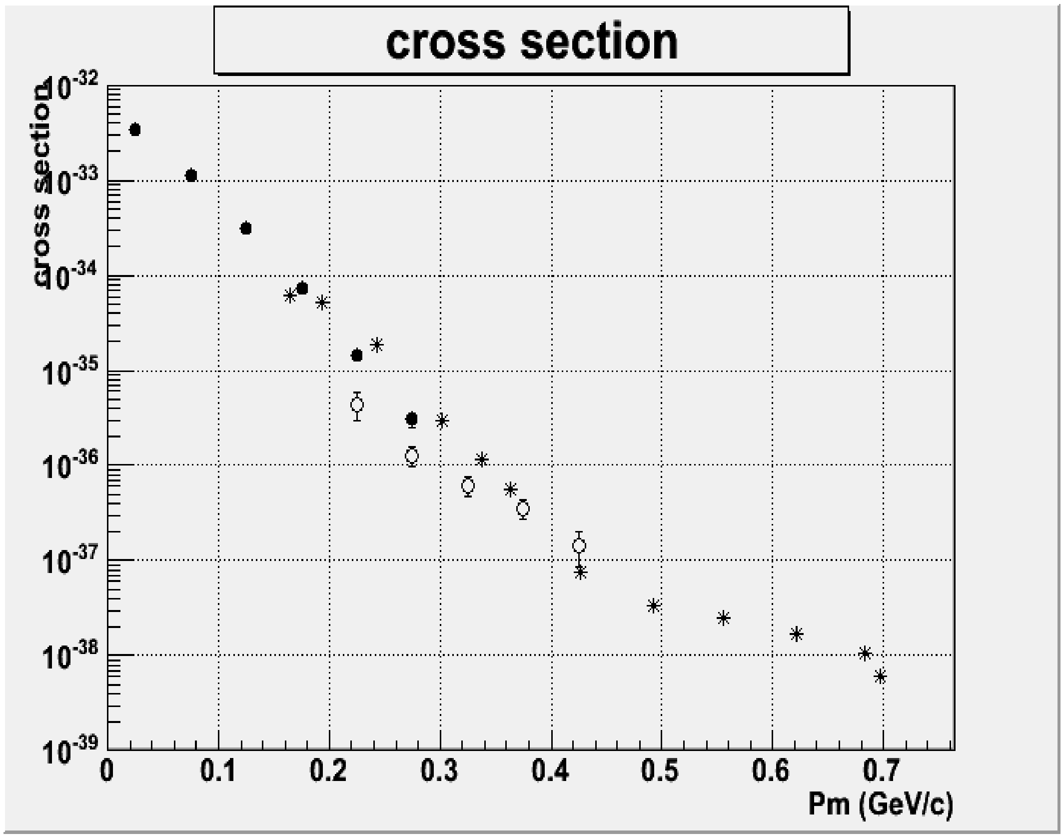

Figure 7.1: Cross Sections for 153 MeV/c (closed dot), 353 MeV/c (open dot) and Theory (asterisk) in cm.^{2}/(MeV$*$SR^2). The first two theory values are underestimates because the theory values we have are only valid above 150 MeV/c, but the simulation continues below 150 MeV/c.

Table 7.1: $^4He(e,e'p)^3H$ average cross sections from equation 5.4 from the Madrid theory [5]. The incident electron energy was 4.4506 GeV, the electron was set at 20.3° and 3.601 GeV/c central momentum. * indicates assuming cross sections for $p_m < 0.153$ GeV/c are equal to the 0.153 GeV/c value.

P_{miss}	θ_p	proton central momentum	$< \sigma >$
GeV/c	degrees	GeV/c	$nb/MeV/sr^2$
0.164*	47.0	1.500	6.19×10^{-2}
0.193*	45.0	1.500	5.19×10^{-2}
0.243	42.5	1.475	1.84×10^{-2}
0.302	40.0	1.449	2.91×10^{-3}
0.338	38.5	1.449	1.15×10^{-3}
0.364	37.5	1.449	5.57×10^{-4}
0.427	35.0	1.417	7.45×10^{-5}
0.492	32.5	1.383	3.33×10^{-5}
0.556	30.0	1.353	2.46×10^{-5}
0.621	27.5	1.308	1.72×10^{-5}
0.684	25.0	1.268	1.07×10^{-5}
0.697	24.5	1.200	6.09×10^{-6}

Table 7.2: Cross Sections in cm.^{2}/(MeV/SR^2)

Pm bin (MeV/c)	153 MeV/c X-section	153 MeV/c $\Delta\sigma_{total}$	353 MeV/c X-section	353 MeV/c $\Delta\sigma_{total}$
0-50	3.38E-033	5.21E-034		
50-100	1.13E-033	1.73E-034		
100-150	3.13E-034	4.82E-035		
150-200	7.18E-035	1.08E-035		
200-250	1.44E-035	2.24E-036	4.40E-036	1.40E-036
250-300	3.06E-036	5.66E-037	1.27E-036	3.02E-037
300-350			6.11E-037	1.38E-037
350-400			3.57E-037	8.62E-038
400-450			1.44E-037	5.90E-038

Table 7.3: 153 MeV/c uncertainties corresponding to each 50 MeV/c bin. Δ Net = $\sqrt{Trues + \Delta T^2}$. Refer to figures 6.2 and 6.3 for an example of Background $_1$ and Background $_2$.

	Background 1	Background 2	Δ Net	Δ Background
0-50	38.2	160.637	94.057	122.437
50-100	562.07	1523.959	245.561	961.889
100-150	588.31	1483.79	229.732	895.48
150-200	311.35	396.386	140.331	85.036
200-250	106.4	153.363	61.704	46.963
250-300	26.1	26.8338	21.567	0.7338

Table 7.4: 353 MeV/c uncertainties corresponding to each 50 MeV/c bin. Δ Net = $\sqrt{Trues + \Delta T^2}$. Refer to figures 6.2 and 6.3 for an example of Background $_1$ and Background $_2$ for 153 MeV/c.

	Background 1	Background 2	Δ Net	Δ Background
200-250	5.5	1.375	9.145	4.125
250-300	12.125	10	13.500	2.125
300-350	1.29162	8.1245	13.913	6.83288
350-400	10.45838	10.6875	12.639	0.22912
400-450	1.83338	0	6.265	1.83338

Table 7.5: General uncertainties

	153 MeV/c value	uncer-tainty in 153 MeV/c	353 MeV/c value	uncer-tainty in 353 MeV/c
radiative correction	1.74869	0.00343	1.75212	0.00343
ΔE	99 MeV	10 MeV	91.5 MeV	10 MeV
N_e	6.809×10^{18}	3.12×10^{16}	1.092×10^{19}	3.12×10^{16}
N_{tgt}	$6.732\mathrm{E}\times10^{22}$	7.678×10^{20}	5.662×10^{22}	6.457×10^{20}
computer livetime	0.91579	0.1	0.94952	0.1
electronic livetime	1	0	1	0
trigger efficiency	0.97	0.01	0.97	0.01
wire chamber efficiency	0.9955	0.001	0.9955	0.001
tracking efficiency	0.9895	0.0075	0.9895	0.0075

CHAPTER 8

Discussion and Conclusion

This measurement is the first with such a high value of x_b and the first to use the Madrid mean field relativistic dynamical theory. In the cross section plot (figure 7.1), the theory is only valid above 150 MeV/c. It would have been prudent on our part to ask the Madrid group [5] for the theoretical cross sections in the low pmiss region where we have data. Also, maybe there's a discrepancy in the cross section because we're not taking into account the real spectrometer acceptance. And we can't take it into account because the simulation doesn't have that capability.

An improvement in the missing momentum acceptance would be to include the spectrometer field map in the geant simulation. This may improve the pmiss xsect matching at pmiss overlap points. However, there was a time constraint and we were not able to perform this correction.

When we use the theory and data cross sections from tables 7.1 and 7.2 and calculate the ratio of the sums from 47 degrees to 35 degrees we find:

$$\frac{\Sigma(\sigma_{data}(\theta_p) * sin\theta_p * d\theta_p)}{\Sigma(\sigma_{theory}(\theta_p) * sin\theta_p * d\theta_p)} = 0.68. \tag{8.1}$$

This result is consistent with $(e, e'p$ results across the nuclear species that there is a smaller cross section measured in the data than mean field theory predicts. This has been interpreted as nucleon correlations redistributing protons from mean field orbits to other configurations. My result is consistent with correlations present in 4He.

There are much data available in the high emiss region which would benefit from detailed analysis of a possible two nucleon absorption peak like in Dr. Benmokhtar's PhD thesis [2]. The Emiss plots for kinematic values 153 and 353 MeV/c, shown in figures 5.2 and 5.3, are examples of such data.

REFERENCES

[1] K. Aniol, F. Benmokhtar, S. Gilad, D.W. Higinbotham, A. Saha spokespersons, Detailed Study of ^4He Nuclei through Response Function Separations at High Momentum Transfers, TJNAF Hall A Proposal e07006.

[2] F. Benmokhtar, Ph.D. thesis, Rutgers (2004).

[3] Computational Fluid Dynamics calculation, private communication with Silviu Covrig.

[4] Eugene Chudakov, private communication

[5] Jose Vignote, private communication

Udias J.M. and Vignote J.R.,2000 *Phys. Rev. C* **62** 034302

Malace S.P. et. al. 2011 *Phys. Rev. Lett* **106** 052501

[6] K. Aniol, Analysis of the SRC target Performance, see

`https://userweb.jlab.org/~aniol/e08009/iscan_corrections/SRCtgt.pdf.`

[7] K. Aniol, GEANT Simulations for E08009, see

`https://userweb.jlab.org/~aniol/e08009/simulations.pdf.`

[8] R.E.J. Florizone, Ph.D. thesis, MIT (1999).

[9] J.L. Herraiz, Ph.D. thesis, Complutense University of Madrid (2010).

[10] M. Rvachev, Ph.D. thesis, MIT (2003).

[11] M. Jones, Report of electronic deadtime, (2000). See

`http://www.jlab.org/~jones/e91011/report_on_deadtime.ps.`

[12] N. K. Liyanage, Ph.D. thesis, MIT (1999).

APPENDIX A

Schwinger calculation for scattering

```
c  from R. Florizone thesis, appendix B

c  Schwinger distribution for real photon emission

c************************************************************

subroutine schwinger(ei,w,th0,atar,ee)

real ei,ef,w,th,me,mtar,atar,b,eta,eta2,Q2

real alpha,radian,pi,snth,snth2,x1,x2,th0

real gamma,beta,r,fact,ee

data pi/3.141592/,radian/57.29578/,alpha/7.2974e-03/

data amu/0.931494/,me/0.511e-03/

ef = ei - w

mtar = atar*amu

c* note it is assumed that the angles are given in radians

th = th0/2.

snth = sin(th)

snth2 = snth*snth

Q2 = 4.*ei*ef*snth2

b = 1. + 2.*w/mtar*snth2

eta = 1. + 2.*ei/mtar*snth2
```

```
eta2 = eta*eta

x1 = ei*ef*b/eta2

beta = log(x1)

x2 = Q2/me/me

gamma = alpha/pi*(log(x2) - 1.)

x1 = beta*gamma

fact = exp(x1)

x1 = 1./2./gamma

r = fact*rand()

ee = ef - r**x1   ! r**x1 is the DeltaE bite in the radiated spectrum


return

end
```